Title
Pre-Eruptive Water Concentrations of Glassy Melt Inclusions From Mount Suswa and Eburru Volcano of the Central Peralkaline Province, Kenya

Author
Jaramillo, Sean Anthony

Publication Date
2021

UNIVERSITY OF CALIFORNIA
RIVERSIDE

Pre-Eruptive Water Concentrations of Glassy Melt Inclusions From Mount Suswa and Eburru Volcano of the Central Peralkaline Province, Kenya

A Thesis submitted in partial satisfaction
of the requirements for the degree of

Master of Science

in

Geological Sciences

by

Sean A. Jaramillo

June 2022

Dissertation Committee:
Dr. Maryjo Brounce, Chairperson
Dr. Heather Ford
Dr. Andrey Bekker

The Thesis of Sean A. Jaramillo is approved:

Committee Chairperson

University of California, Riverside

Acknowledgements

This research was supported by NSF EAR1849700. I would like to thank Dr. Tobias Fischer of the University of New Mexico for providing us with our samples from Africa. I would also like to thank Dr. Brian Damiata of the University of California, Los Angeles for the assistance and access to the UCLA microprobe. Also, I would like to thank Jen Humphreys of the University of California, Riverside for their help at the UCLA microprobe and for their general help during the thesis writing process. Additionally, I would like to thank Dr. Elizabeth Anthony for suggestions on where to take this project, and for providing much of the background knowledge for Eburru. Finally, I would like to thank Dr. Maryjo Brounce for being both a teacher and mentor through my undergraduate and graduate career.

ABSTRACT OF THE DISSERTATION

Pre-Eruptive Water Concentrations of Glassy Melt Inclusions From Mount Suswa and Eburru Volcano of the Central Peralkaline Province, Kenya

by

Sean A. Jaramillo

Master of Science, Graduate Program in Geological Sciences
University of California, Riverside, June 2022
Dr. Maryjo Brounce, Chairperson

There is a large swath of slow seismic velocities in the upper mantle underneath the East African Rift, centered under the Main Ethiopian Rift segment. The presence of melts, H_2O, or CO_2 in the mantle can slow seismic velocities as well as lower mantle solidus, generating melts at higher pressures and lower temperatures than dry, carbon-free mantle. The volatile content of the mantle in the southern portion of the rift remains unconstrained, as the lithosphere is thick there, which leads to substantial differentiation during the formation of magmas and eruption of evolved, alkalic lavas that are difficult to link directly to the composition of the mantle. To understand the differentiation process, the water content of alkalic magmas erupted in this area has been constrained, and the H_2O source whether from the asthenospheric mantle or lithospheric mantle and/or crustal assimilation has been tested. Major and volatile element concentrations of feldspar-hosted melt inclusions from tephras erupted at Suswa and Eburru have been measured to help understand the formation history of highly evolved magmas of the Central Peralkaline Province. The Suswa melt inclusions are in phonolites with 0.2-1.9 wt% H_2O, while the Eburru melt inclusions are in trachytes with 3.45 to 5.80 wt% H_2O. The Eburru trachytes are best described by the fractional crystallization of a dry (0.25 wt% H_2O) basalt, assimilating the Pan-African crust after ~55% (by mass) of fractional crystallization. The assimilation resulted in the high-water content of Eburru magmas, as measured directly in melt inclusions. The history of Suswa phonolites is best explained by the fractional crystallization of a high-alkali basalt, though this model alone does not account for the whole range in major element composition. There is a shallow negative slope between SiO_2 and Na_2O+K_2O contents in the Suswa melt inclusions and whole-rock concentrations that is best explained by magma mixing between an evolved Eburru-like magma and a Suswa-like evolved magma with higher alkali concentrations. The combination of fractional crystallization, magma mixing, and crustal assimilation is deemed essential for the development of the diverse and evolved magmas of the Central Peralkaline Province in East Africa.

Table of Contents

List of Figures

List of Tables

INTRODUCTION

Plate tectonics has occurred on Earth for at least ~2.0 billion years (e.g., Condie and Kroner, 2008), leading to repeated supercontinent cycles over geological time with continental rifting, the formation of ocean basins, the destruction of ocean basins through subduction, and continental reassembly. Despite the ongoing and important nature of plate tectonic processes, the understanding of how the first stage of the process begins and develops - the rifting of continents - is limited. For example, the combined forces of ridge push, slab pull, and asthenospheric drag are not of a magnitude high enough to disrupt strong continental lithosphere (Forsyth and Uyeda 1975), suggesting that the continental lithosphere must be weakened somehow before continental rifts can develop (Buck 2004). Intrusion of magma into the continental lithosphere is one way to do this and can explain the presence of large igneous provinces in regions of continental rifting. One such example is the African-Arabian continental flood basalt province located in the East African Rift Zone. However, mantle melt originating from decompressional melting should be limited under a relatively thick continental lithosphere, where the average thickness of continental lithosphere ~160 km (Pasyanos 2010) corresponds to pressures near 5 GPa, requiring mantle temperature above 1600˚C to initiate anhydrous melting (Hirschmann et al., 2009). To generate relatively large volumes of magma in mantle cooler than this at the base of unstretched continental lithosphere, the mantle would likely need to contain elevated levels of CO_2 and H_2O.

The East African Rift zone is a Miocene-aged series of rift valleys that extends for ~ 6000 kilometers from the Gulf of Aden to Mozambique (Dobrynina et al., 2017). It splits into two branches at the northern Tanzanian Craton, generating the amagmatic/sparsely magmatic Eastern Branch in Tanzania and Kenya and the magmatic Western Branch in Uganda and The Democratic Republic of Congo. The oldest evidence of extension are the Getra-Kele alkali basalts, which erupted between 19 and 11 million years ago (Ebinger et al., 1993, George and Rogers, 2002). Petrologic studies of Southern Ethiopian flood basalts revealed that the average temperature of the upper mantle is elevated by 140°C (approximately 1490°C) compared to ambient mantle (as sampled by mid-ocean ridge basalts) (Rooney et al., 2012). While this is above the ambient mantle temperature, it is much cooler than so-called hot spots such as Hawaii (average potential temperature 190°C above ambient mantle, approximately 1540°C using the same geothermometers, e.g., Rooney et al., 2012). This is somewhat at odds with expectations of melting dry mantle rock at high pressures, which requires hotter mantle temperatures than seen at the rift (see above), as well as with geophysical observations of the mantle under the East African Rift. There is a large (approx. 500 km wide, Fig 1) low seismic velocity region present in the upper mantle under the rift, with seismic wave velocities that are among the lowest in the world ($\Delta V_S \sim -10\%$, Emry et al., 2019). Typically, slow seismic wave velocities are explained by anomalously hot mantle (e.g., Hawaii; Karato and Jung, 2003), mantle that itself has has elevated H_2O and/or CO_2 contents in the solid rock (e.g., the Marianas; Jackson and Faul, 2010), or the presence of melt in the mantle (including melt produced by virtue of the presence of H_2O and/or CO_2 itself; Jackson and Faul, 2010). The warm, but not hot, temperatures of the mantle under the rift alone are not sufficient to explain these slow seismic wave speeds.

Other factors may contribute significantly to the observed geophysical anomalies in this region. For example, the H_2O and CO_2 contents of the solid mantle rock (i.e., in the absence of any melt) are not well known along the rift and elevated concentrations of either component may slow seismic wave speeds significantly (Jackson and Faul, 2010). Compounding this, the presence of elevated H_2O and/or CO_2 contents could also lead to increased melt generation (Dasgupta and Hirschmann, 2007), and the presence of melt is also thought to slow seismic wave speeds (Jackson and Faul, 2010). Alternatively, the presence of the Afar superplume in this region (Bastow et al., 2008) could suggest that there could be recycled materials in the form of pyroxenite and eclogite (i.e., the metamorphic rock assemblages that result from subducting oceanic crust into the deep mantle) entrained in the plume and thus brought to the zone of melting in the upper mantle of this region. These lithologies typically melt at lower temperature than peridotite mantle rock at the same pressure (Kogiso et al., 2004), again contributing to the presence of melt in the mantle under the East African rift, which could slow seismic wave velocities (e.g., Rooney et al., 2012, Dasgupta and Hirschmann, 2007, Jackson and Faul, 2010). Combined, the moderate nature of the inferred temperature anomaly of the mantle under the East African Rift and the extreme slowness of seismic waves suggest that there may be a strong role for H_2O, CO_2, and/or pyroxenite/eclogite in the upper mantle.

Despite this, there are relatively few measurements of dissolved CO_2 and H_2O contents in volcanic rocks from along the rift. Olivine-hosted melt inclusions from Erta Ale in the Afar region have measured low H_2O and CO_2 contents, 0.08 to 0.13 wt% H_2O and 0 to 201 ppm CO_2, suggesting a damp or dry mantle in the northern parts of the rift

(Field et al., 2012). In the same region, olivine and plagioclase-hosted melt inclusions from Nabro Volcano have higher concentrations, from 0.1 to 2.1 wt% H_2O and 0 to up to 3455 ppm CO_2, but these are measured in relatively evolved andesite and dacite compositions and are difficult to link directly to concentrations of either in the mantle source (Donovan et al., 2018). Alkali feldspar-hosted melt inclusions from Dabbahu, also from the Afar region, report a range of 2.2 to 5.8 wt% H_2O, 6 to 462 ppm for CO_2, though like Nabro, they are from evolved magmas and may not directly represent the composition of the mantle (Field et al., 2012). Nepheline melt inclusions from Oldoinyo Lengai volcano in Tanzania have a wide range of H_2O and CO_2 contents, 0.1 to 3.1 wt% H_2O and 2.7 to 8.7 wt% CO_2 (de Moor et al., 2013). Olivine-hosted melt inclusions from Nyamuragira volcano in the western branch yield H_2O concentrations from 0.6 to 1.4 wt% and CO_2 from 350 to 1900 ppm (Head et al., 2011). These observations, from volcanoes far to the north (e.g., Nabro), to the west (e.g., Nyamuragira), and from nearby (e.g., Oldoinyo Lengai), broadly demonstrate H_2O contents higher than expected from the nominally dry upper mantle (e.g., mid-ocean ridge basalts typically have 0.1 to 0.75 wt% H_2O; Dixon et al., 2002), however constraints on volcanoes outside of the Afar region are limited and whether the H_2O and CO_2 contents of the mantle are evenly distributed throughout the mantle under the rift remains unclear. These observations are found in melt inclusions ranging from olivine to nepheline, obscuring the relative importance of differentiation on the high water contents in this region. The Pan African Lithosphere also varies in thickness from essentially nonexistent in the far eastern portions of the Gulf of Aden where magmas erupt that are very similar to mid-ocean ridge basalts, to as thick as the Tanzanian Craton (~ 150 km according to surface wave models of Fishwick et al., 2010) in the south. The Pan African Lithosphere defined by Schilling et al., (1992) is a fictive rock that is required to explain the radiogenic isotopic compositions of submarine glasses erupted in the Gulf of Aden. Whether this component is comprised of the crust or mantle portion of the Pan African Lithosphere is unspecified. Because some lavas that erupt are very evolved, it is plausible that there is substantial amounts of crustal melting and assimilation as well as mixing of magmas at various stages of their cooling and crystallization trajectories prior to eruption. The behavior of water in the magmas that participate in and are formed as the result of these melting, assimilation, and mixing processes is unknown. So, in addition to uncertainties in the water contents of the mantle under the East African Rift, many questions remain about the water contents of the thick and ancient African crust/mantle lithosphere. What is the amount of water that is sourced from the asthenospheric mantle and what is the amount that is sourced from lithospheric contamination, and what is the combined result of substantial crystallization, lithospheric contamination, and magma mixing on water contents of the final erupted lavas? The answers to these questions are paramount to isolating the water contents of the asthenospheric mantle with confidence.

Here, we will explore the behavior and role of H_2O during differentiation of these evolved magmas from the Central Peralkaline Province in Kenya. We present new measurements of volatile and major element concentrations of naturally glassy feldspar-hosted melt inclusions, as well as their feldspar hosts and matrix glass adhered to the outside of the phenocryst hosts, taken from Mount Suswa and Eburru Volcano in Kenya.

We use these measurements to model differentiation of magmas in the Central Peralkaline Province. We quantify the effects of extensive crystal fractionation using the thermodynamic model MELTs, use MELTs to infer what is necessary for the extent of assimilation of the crust, and quantify the role of magma mixing during various stages of differentiation to understand the roles of water in the creation of variable compositions of broadly evolved magmas in this region.

Geological setting and prior work

Mount Suswa

Mount Suswa is a shield volcano located in the Central Kenya Peralkaline Province along the Kenyan branch of the East African Rift Zone. Other volcanoes in the Central Kenya Peralkaline Province are Eburru and Elmenteita, with Tandamara further north and lava compositions vary dramatically from basalt to high-alkali phonolites, trachytes and rhyolites across this province (Figure 2). Lavas erupted from Mount Suswa specifically are broadly trachytic to phonolitic in composition (Figure 2; White et al., 2012). The eruption history is divided into two phases, the pre-caldera/syn-caldera and the post-caldera phase. The first phase represents lavas erupted during the formation of the main volcanic edifice as well as the first caldera collapse. The rocks associated with these eruptions are mostly peralkaline trachyte ranging from silica-saturated to silica undersaturated in composition (White et al., 2012). The second phase represents lavas erupted soon after the collapse of the caldera and during the formation of a second smaller caldera. These rocks are mostly peralkaline phonolites (White et al., 2012). The samples studied here are from the youngest eruption event, called the Ring Trench Group, and are made up of phonolites erupted during the formation of the second caldera.

The main mineralogical phases of the Ring Trench group include both high potassium feldspars ($An_{0–5}Ab_{50–60}Or_{30–40}$) and sodic feldspars ($An_{3–15}Ab_{65–70}Or_{15–20}$ White et al., 2012). These feldspars show oscillatory zoning with respect to Ca and K. Additionally, the phonolites contain feldspathoids minerals, like nepheline and sodalite.

Eburru Volcano

Eburru is a 470 km^2 volcanic complex located northwest of Lake Naivasha in Central Kenya. Lavas erupted from Eburru range from trachytic to pantelleritic in composition (Ren et al., 2006; Clarke, 1990). The oldest volcanic activity in the region is displayed as two ring structures primarily composed of pantelleritic lavas, pyroclastic deposits and welded tuff. Following this were two eruptions of the Eburru Trachyte Formation between 1.2 and 0.4 Ma (Ren et al., 2006). These events deposited trachyte lava flows, pumice, scoriaceous rocks and welded pyroclastic rocks. The most recent volcanic event erupted the Eburru Pantellerite Formation. The formation is made up of pantellerite lava flows and obsidian deposits that extend north to Elmenteita.

Sample Descriptions

Mount Suswa

The tephra examined in this study ranges in color from black to brown, and are naturally glassy, vesicular (<50%), and subangular. The potassium feldspar crystals found in the tephra are 1-2 cm in diameter, white to brown, prismatic and anhedral to subhedral. The feldspar grains contain several melt and fluid inclusions. Additionally, black spherical sulfide blebs (<10 μm to 30 μm diameter) are present within the grains and dispersed throughout. The naturally glassy melt inclusions are rectangular, tabular and light brown in color and range in size from ~20 μm to ~160 μm. They range in shape from oblate/spherical to more rectangular. Typically, glass inclusions contain between zero and four vapor bubbles. The fluid inclusions are small (<10 μm), transparent, and spherical and are dispersed throughout the grains in no particular pattern.

Eburru Volcano

The tephra is black in color, naturally glassy, vesicular, and subangular. The potassium feldspar crystals found in the tephra are 0.5-1 cm in diameter, white, tabular and subhedral. The feldpar grains contain several melt inclusions. The inclusions are naturally glassy, rectangular to tabular and light brown in color and range in size from ~20 μm to ~100 μm. They range in shape from elongated ovals to more rectangular/square. Some of the glass inclusions contain one to two vapor bubbles. There are no discernible fluid inclusions or sulfides present within this sample.

Methods

Glass inclusions contained in feldspar crystals were exposed at the surface via optical polishing for electron probe microscope analysis (EPMA). These EPMA analyses were conducted using a JEOL-8900 five-spectrometer microprobe at the University of California Los Angeles. During major element analysis of the glass, the beam was operated at 15 nA for Suswa, 10 nA for Eburru, with an accelerating voltage of 15 kV and a 10 µm beam diameter. The elements Ca, Si, Na, Fe, K, Ti, Al, Mg, Mn, and P were measured for Suswa with 20-40 s peak count times and 5-20 s background count times. The elements Ca, Si, Na, Fe, K, Ti, Al, Mg, Mn, and P were measured for Eburru with 10-20 s peak count times and 5 s background count times. All data were subject to ZAF correction procedures. Primary calibration standards include anorthite, albite, magnetite, potassium feldspar, sphene, forsterite, manganese, and Durango apatite. The alkalic, hydrous, and high-Si nature of both Eburru and Suswa samples likely led to evaporation of Na and K (i.e., alkali loss) during analysis. For this reason, all Na and K determinations should be taken as minima. Sulfur and chlorine were measured separately using a beam operated at 80 nA, an accelerating voltage of 15 kV and 10 µm beam diameter. Eburru samples were too alkali rich to be measured for S and Cl without electronic damage to the samples because of the high operating beam current necessary for accurate analysis. Primary calibration standards include pyrite, synthetic barium apatite, barite, and Ba-Cl apatite. For the hosts, a focused electron beam was operated at 15 nA and an accelerating voltage of 15 kV. Anorthite, titanium albite, magnetite, potassium feldspar, sphene, forsterite, manganese, and Durango apatite were used as primary calibration standards.

After EMPA of melt inclusions, their mineral hosts, and any analyzable matrix glass adhered to the outside of the grains, all sample pits were polished away, being careful to account for possible beam damage within the activation volume of each EMPA spot. Melt inclusions were then polished from the opposite side until doubly exposed. All samples were washed gently with acetone to remove all epoxy residues. Dissolved H_2O and CO_2 concentrations in glass inclusions were analyzed by Fourier-transform infrared (FTIR) spectroscopy at the University of California Riverside. All samples were analyzed using Thermo Scientific Nicolet iS50 Fourier-transform infrared spectrometer with a Nicolet Continuum Fourier-transform infrared microscope attachment. Spectra for samples were collected between 1000 and 6000 cm^{-1} using a tungsten-halogen source, KBr beamsplitter and a liquid-nitrogen cooled MCT-A detector. Some samples were measured from 1000 cm^{-1} to 4000 cm^{-1}. The bench, microscope, and samples were continuously purged by air free of water and carbon dioxide using a Whatman purge-gas generator. Aperture dimensions were selected for each sample depending on the geometry of free glass pathways, ranging in size from 15 x 15 µm to 90 x 149 µm. Dissolved total H_2O concentrations were determined using the 3530 cm^{-1} band where possible. In some cases, the 3530 cm^{-1} band was saturated. In this case, the 1630 cm^{-1} band attributed to molecular H_2O was used in conjunction with the experimental work of (Dixon et al., 1995) to calculate total H_2O concentrations.

We measured $S^{6+}/\Sigma S$ ratios of the melt inclusions by micro-X-ray absorption near-edge structure (µ-XANES) spectroscopy at beamline 13-IDE, Advanced Photon Source, Argonne National Laboratory. Spectra were collected in fluorescence mode from 2447 eV to 2544 eV, with a dwell time of 2 seconds on each point, using a Si [111] monochromator and a defocused beam diameter of 20 µm. Counts were recorded on a multi-element silicon drift detector x-ray spectrometer, equipped with two Si drift diode detectors. All analyses were done in a helium atmosphere to avoid interaction between the incident photon beam and atmosphere. Incident beam intensity was attenuated using several layers of aluminum foil yielding a photon dosage on the order of ~5 x 10^9 photons per second per μm^2, reflecting a balance between the intensity required to produce interpretable S-XANES spectra from materials with low S-abundances (i.e., <1000 ppm) and the mounting evidence that very high photon density fluxes electronically damage Fe and S in silicate materials. Each analysis was performed using a stationary beam. Spectral merging, background subtraction, and normalization for these spectra was done using the X-ray absorption spectroscopy data software package ATHENA (Ravel and Newville, 2005), applied uniformly to all spectra so that the region from 2447-2462 eV varies around a value of 0 and region from 2485-2457 varies about a value of 1. These normalized spectra were then subject to spectral fitting routines using the Peak Analysis (PAN) software package. Each normalized spectra was fit between 2462-2487 eV with four Gaussian curves – one for the background (peak center fixed at 2485 eV) and one each for sulfate (peak center fixed at 2481 eV), the broad sulfide feature (peak center fixed at 2477 eV), and the narrow sulfide feature (peak center fixed at 2470 eV). The integrated $S^{6+}/\Sigma S$ ratios were calculated using the area under the curve of the 2485 eV peak divided by the area under the curve of the 2477 eV peak.

Results

Major and volatile elements

Feldspar hosts of Suswa range in composition from $An_{5-13}Ab_{65-67}Or_{18-30}$ (Table 1). The matrix glasses adhered to the outside of some of the feldspar range in composition from 55.6 to 57 wt% SiO_2, 0.92 to 0.98 wt% TiO_2, 7.2 to 7.4 wt% FeO*, 13.3 to 13.8 wt% Na_2O + K_2O, 572 to 580 ppm S and 1580 to 1730 ppm Cl (Table 2). Melt inclusions are phonolitic in composition (Figure 2) and have 6.8-7.8 wt% FeO* and 0.94-1.4 wt% TiO_2 (Figure 3A, B, Table 2). The Suswa melt inclusion compositions reported here overlap with the low end of the range of SiO_2 contents and extend to lower SiO_2 contents than those reported for whole rock analyses of Suswa rocks and overlap entirely with the FeO* and TiO_2 contents of the Suswa whole rocks (Figure 2, 3A, B; White et al., 2012). Within the suite of Suswa melt inclusions, SiO_2 contents are uncorrelated with NA_2O+K_2O, FeO* and TiO_2 (Fig 3A, B). The Suswa whole rocks and melt inclusions together have lower SiO_2 than Eburru melt inclusions (discussed below) and overlapping SiO_2 with whole rock analyses of lavas from nearby volcanoes Elmenteita and Tandamara, though Suswa rocks are significantly more alkali rich than Elmenteita and Tandamara whole rocks (Figure 2). The H_2O contents of Suswa melt inclusions range from 0.2 to 1.9 wt%, Cl contents from 1460 to 1890 ppm and S contents from 540 to 812 ppm. The H_2O contents do not correlate with S, Cl, K_2O or SiO_2 (Fig 4A-D). The S contents of the melt inclusions do not correlate with Cl, are positively correlated with FeO* and negatively correlated with SiO_2 (Fig 5A-C). The CO_2 concentrations of these melt inclusions are below the detection limits by FTIR.

The matrix glass adhered to the outside of the Eburru feldspar crystal has a composition of 65.96 wt% SiO_2, 0.50 wt% TiO_2, 9.32 wt% FeO* and 12.09 wt% Na_2O + K_2O (Table 3). Eburru melt inclusions are trachytic in composition (Figure 2) and have 6.64-8.8 wt% FeO*, and 0.15-0.59 wt% TiO_2 (Table 3). Within the suite of melt inclusions studied here, SiO_2 contents of the melt inclusions are uncorrelated with Na_2O+K_2O, FeO*, and TiO_2 (Fig 2; 3A, B). The H_2O contents of Eburru melt inclusions range from 3.45 to 5.80 wt%. The H_2O contents do not correlate with K_2O or SiO_2 (Fig 4A, 4C). The CO_2 concentrations of these melt inclusions are below the detection limits by FTIR. Taken together with the whole rock analysis of other Central Kenyan Peralkaline lavas and the melt inclusion analyses of Suswa, there is a positive correlation between SiO_2 and Na_2O+K_2O for Tandamara and Elmenteita whole rocks, a slight negative correlation between SiO_2 and Na_2O+K_2O for Suswa and Eburru whole rock and melt inclusion analyses, and a negative correlation across all samples between SiO_2 and TiO_2. Eburru melt inclusions define the most silica-rich compositions, and whole rock analyses of Elmenteita lavas define the lowest silica compositions.

Within each suite of melt inclusions at Eburru and Suswa, H_2O and K_2O are uncorrelated. However, taken together, there is a slight negative correlation between H_2O and K_2O, where Eburru samples have slightly lower K_2O contents and higher H_2O contents (Fig 4A). We caution against interpretations of this phenomenon because of the likelihood of alkali loss during analysis of these very alkalic, hydrous, and silica rich samples (see Methods section, above). Similarly, H_2O and SiO_2 are uncorrelated within the suite of inclusions, but taken together are positively correlated, with Eburru inclusions having higher H_2O and SiO_2 compared to Suswa samples (Fig 4C).

The oxidation state of sulfur

The S-XANES spectral forms for Suswa inclusions reveal peaks at 2469, 2476, and 2482 eV, indicating that sulfur is present as both S^{2-} and S^{6+} (Fig 6). These spectral variations correspond to variability in the oxidation state of S dissolved in Suswa melt inclusions that range in $S^{6+}/\sum S$ (i.e., $S^{6+}/(S^{6+} + S^{2-})$) from 0.05 to 0.16 (Table 4). These $S^{6+}/\sum S$ ratios do not correlate with S or H_2O (Fig 7).

Discussion

The oxidation state of sulfur and fO_2

We calculated oxygen fugacities (fO_2) relative to the quartz-fayalite-magnetite oxygen buffer of Suswa melt inclusions from measured $S^{6+}/\Sigma S$ ratios using the calibration of Jugo et al. (2010), yielding a range of fO_2 between ΔQFM=+0.4 to +0.7 (Table 4). This calibration is based on silicate melts that are basaltic in composition, which are significantly different from the phonolites of Suswa studied here. Accordingly, we also calculated fO_2 relative to the ΔQFM buffer of Suswa melt inclusions from measured $S^{6+}/\Sigma S$ ratios using the calibration of Klimm et al., (2012), yielding a range of fO_2 between ΔQFM -0.7 and -0.4 (Table 4). This calibration is based off albitic glasses and thus is somewhat closer to capturing the importance of alkali elements like K and Na in calculating fO_2 from measured redox parameters, which is important for Suswa phonolites. Finally, we calculated fO_2 relative to the QFM buffer by calculating $Fe^{3+}/\Sigma Fe$ ratios from our measured $S^{6+}/\Sigma S$ ratios according to the modified relationship between Fe-S redox pairs described by Muth et al. (2021). The calculated $Fe^{3+}/\Sigma Fe$ ratios of Suswa melt inclusions range from 0.16 and 0.18 and correspond to fO_2s calculated using the calibration of Kress and Carmichael (1991) of between -0.4 and -0.1 (Table 4). There are uncertainties in each approach, but because the experimental library considered by Kress and Carmichael include alkalic natural rock compositions similar to the Suswa phonolites, we prefer those values (ΔQFM -0.4 to -0.1).

These calculated oxygen fugacities are similar to that recorded by mid-ocean ridge basalts and lower than typical arc and back-arc basalts and rhyolites, as well as lower than ocean island basalts from Hawaii, Iceland, the Canary Islands, and Mount Erebuys (e.g., see Cottrell et al., 2021). These oxygen fugacities are also similar to that recorded by melt inclusions (Brounce et al., 2022) and olivine grains (Nicklas et al., 2022) from Reunion Island. This is notable because the Reunion mantle plume is, like the Afar mantle plume, a “C” or “FOZO” plume (e.g., see Brounce et al., 2022 and references therein), and is expected to record similar fO_2s to the normal upper mantle sampled by mid-ocean ridge basalts. That the very evolved rocks studied here also record low oxygen fugacities indicates that whatever the course of crystallization, crustal assimilation, and various magma mixing processes, the net impact on the fO_2 of the magmas sampled by the melt inclusions studied here is to maintain fO_2s like that of the depleted upper mantle. In other words, the differentiation processes we describe below will not have changed the fO_2 of these magmas.

Crystallization and degassing

We modelled the pressures of entrapment of our melt inclusions and the effects of volcanic degassing using DCOMPRESS (Burgisser et al., 2015). According to DCOMPRESS, the measured H_2O-S contents of Suswa melt inclusions are consistent with pressures of entrapment of 150 to 400 bar, which correspond to depths in the crust of 450 to 1200 meters. Volcanic degassing of a CHOS gas from a phonolitic magma at 900°C, ΔQFM ~ +0.7, an initial H_2O content of either 1.9 wt% (Figure 4B, blue curve) or 0.8 wt% H_2O (Figure 4B, green curve) from an initial total pressure of 400 bar to a final pressure of eruption of ~ 1 bar leads to a decrease in both H_2O and S contents that is not seen in Suswa samples (Figure 4). Both models degas from their initial H_2O and S concentrations to <0.5 wt% H_2O and <150 ppm S. The Suswa samples lie above the modeled degassing paths indicating that they do not capture H_2O or S degassing. This means that the measured H_2O and S contents of Suswa melt inclusions likely reflect their values during differentiation in the crust and can be used to assess how H_2O changes during these complex processes. For Eburru melt inclusions, we used VolatileCalc (Newman and Lowenstern, 2002) to measure pressures of entrapment assuming 0 ppm CO_2 and using the rhyolite solubility model. At 900°C, Eburru melt inclusions are consistent with pressure of entrapment of between 874 to 2019. These pressures are significantly higher than those of Suswa and correspond to depths in the crust of 2662 to 6057 meters.

We modelled the effects of fractional crystallization on residual magma compositions of Suswa using the Rhyolite-MELTs model of Gualda et al. (2015). The model used a starting pressure of 1000 bar and $Fe^{3+}/\Sigma Fe$ equal to 0.18. The starting concentration of basaltic sample ES12 of Elmenteita (White et al., 2012) was not sufficient on its own to model the crystallization of the high alkali Suswa melt inclusion samples so new Na_2O (~4.5 wt%) and K_2O (~1.8 wt%) concentrations were chosen. The sample ES 12 was chosen initially to test if there could be a crystallization model using initial compositions of more mafic magmas erupted at the Central Peralkaline Province. The model (blue curves, Fig 8A-E) modeled the effects of fractional crystallization on a cooling magma from a liquidus temperature of 1167°C to ~800°C. This model also began with a starting magma H_2O content of 0.5 wt%. The blue curves on figure 8 panels a-e demonstrate the effect of crystallizing olivine, clinopyroxene, feldspar, and small amounts of nepheline, leucite, spinel, apatite and whitlockite. As SiO_2 increases along these model curves, Na_2O+K_2O increases, TiO_2 decreases, Al_2O_3 increases and FeO* decreases. Water contents also increase, reaching a value of 1.3 wt% by 60 wt% SiO_2, a good match to our new measurements of melt inclusions from Suswa. This model also reproduces well the Na_2O+K_2O and FeO* contents of Suswa melt inclusions but does not match Al_2O_3 and TiO_2 contents.

We modelled the effects of fractional crystallization on residual magma compositions of Eburru using the Rhyolite-MELTs model of Gualda et al. (2015). Two MELTs models were created. Both models used a starting pressure of 1000 bar, $Fe^{3+}/\Sigma Fe$ equal to 0.20, and a starting concentration equal to that of basaltic sample ES12 from Elmenteita (black and red curves, Fig 8A-E; White et al., 2012). The first model (black curve, Fig 8A-E) modeled the effects of fractional crystallization on a cooling magma from a liquidus temperature of 1133°C to ~800°C. This model also began with a starting magma H_2O content of 1.0 wt%. The black curves on figure 8 panels a-e demonstrate the effect of crystallizing feldspar, clinopyroxene, and olivine, and small amounts of apatite, spinel, and FeTi oxides. As SiO_2 increases along these model curves, Na_2O+K_2O increases, TiO_2 decreases, Al_2O_3 does not change significantly and FeO* decreases. Water contents also increase substantially, reaching a value of 4.3 wt% by 65 wt% SiO_2, a good match to our new measurements of melt inclusions from Eburru. This model also reproduces well the Na_2O+K_2O, Al_2O_3, TiO_2 contents of Eburru melt inclusions, but does not match FeO* contents. The mismatch between the model FeO* and melt inclusion FeO* is likely due to too abundant FeTi oxide crystallization, which is promoted in hydrous magmas.

In order to suppress the crystallization of FeTi oxides and provide a better fit to our melt inclusion measurements, we ran a second MELTs model. This model was run identically to that described above, except that the starting magma began with 0.25 wt% H_2O instead of 1.0 wt% H_2O. The liquidus temperature of this modelled magma is 1178°C and the fractional crystallization model was run to cool this magma to ~800°C (red curve, Fig. 8a-e). Like in the model described above, this model results in the crystallization of feldspar, clinopyroxene, and olivine, and small amounts of apatite, spinel, and FeTi oxides, and new in this new model, whitlockite. Also like the model described above, as SiO_2 increases along the model curve, Na_2O+K_2O increases, TiO_2 decreases, Al_2O_3 increases and FeO* decreases. This model curve is a better match to the FeO* contents (and to the other major element contents) of our Eburru inclusions. However, H_2O contents of this model melt do not increase above a value of 1.7 wt%, a factor of ~3 too low according to our direct measurements of the H_2O contents of our Eburru melt inclusions (Fig 8b). Because the model that begins with 0.25 wt% H_2O provides a good fit to all of the major element compositions of our Eburru melt inclusions, we conclude that in order to produce the trachytic compositions of these inclusions from a basalt, crystallization must proceed largely at low H_2O contents. Increasing the starting magma H_2O contents to 1 wt% H_2O promotes the crystallization of too great a mass of FeTi oxides, driving the FeO* content of the residual magma to values lower than observed at these SiO_2 contents. In order to obtain the high water contents we observe in Eburru inclusions, we hypothesize that water must be added to magma at some time after substantial crystallization and prior to eruption.

We assess this possibility (the mixing of a low-H_2O melt with a melt of the hydrated Pan African Lithosphere, at depths at or below which the melt inclusions were entrapped) quantitatively by calculating the H_2O content of a partial low degree melt of the Pan African lithosphere, and mixing it in small proportions (so as not to disturb the major element concentrations significantly) with the dry trachytic MELTs model melts. Using measurements of H_2O in Gulf Aden pillow glasses, previously measured radiogenic isotopic compositions of the same glasses, and a three-component mixing model (Rooney et al., 2012; Schilling et al., 1992), Scoggins (2022) calculate that the Pan African lithosphere contains between 0 and 0.4 wt% H_2O. Using the highest H_2O content determined for Pan African lithosphere of 0.4 wt% (Scoggins, 2022) and $D_{H2O}{}^{rock/melt}$ = 0.012, we calculate that a 0.1% melt of Pan African lithosphere would have H_2O contents of ~31 wt%. We mixed this low degree melt of Pan African lithosphere into our modeled MELTs magma for Eburru (starting water content of 0.25 wt% H_2O) after 55% crystallization, in 1% increments. To match the measured H_2O contents of Eburru melt inclusions in this study (3.45-5.80 wt% H_2O), we require a mixture of 8-15% of the 0.1% melt of the Pan African Lithosphere with ~31 wt% H_2O with 85-92% of the modeled MELTs magma for Eburru. We also calculated the same scenario but for a Pan African lithosphere that contains 0.3 wt% H_2O. A 0.1% melt of this lithosphere using the same $D_{H2O}{}^{rock/melt}$ would have ~23 wt% H_2O. Mixing this melt of Pan African Lithosphere into the same modeled MELTs magma for Eburru requires a 10-21% mixture of the low degree melt of the Pan African lithosphere and 79-90% of the modeled MELTs magma for Eburru to match our H_2O measurements for Eburru melt inclusions. Finally, we calculated the same scenario but for a Pan African lithosphere that contains 0.17 wt% H_2O. A 0.1% melt of this lithosphere using the same $D_{H2O}^{rock/melt}$ would have ~13 wt% H_2O. Mixing this melt of Pan African Lithosphere into the same modeled MELTs magma for Eburru requires a 20-38% mixture of the low degree melt of the Pan African lithosphere and 62-80% of the modeled MELTs magma for Eburru to match our H_2O measurements for Eburru melt inclusions. Of these three calculations, the mix of 20-38% Pan African Lithosphere at 1.7 wt% H_2O is the least likely, as mixing larger amounts of the Pan African Lithosphere with the Eburru melt likely will cause changes in major element compositions (i.e. increases in SiO_2 beyond which our data set indicates), for which there is limited evidence in our measurements or those from the literature (i.e., the observed major element compositions can be recreated through simple fractional crystallization). We cannot recommend between the two mixtures of Pan African lithosphere containing 0.3 and 0.4 wt% H_2O, as both reach the lowest water concentrations of the Eburru melt inclusions (3.45 wt% H_2O) as are thus both plausible within the constraints our study provides. However, we point out that the first scenario mixing of a 0.1% melt of Pan African lithosphere containing 0.4 wt% H_2O requires the least mixing in of an unknown component and if true, would be most likely not to perturb the major element compositions of the produced mixed magma, the composition of which can otherwise be explained through simple crystal fractionation.

Finally, we note that on a diagram of Na_2O+K_2O versus SiO_2, the lavas of Suswa and Eburru in sum display a shallowly sloped negative relationship that cannot be produced by fractional crystallization of known mineral phases with stabilities in magmas like that of either Suswa or Eburru, and thus indicates the possibility of mixing of magmas during the crystallization events described above. We modelled the effects of magma mixing on residual magma compositions of Suswa and Eburru using the Rhyolite-MELTs model of (Gualda et al., 2015). Mixing line compositions were chosen to be evenly spaced out within the MELTs curves of Suswa and Eburru (Fig 9). There are essentially unlimited combinations of melt compositions along these two model curves that could be mixed together to yield hybrid composition magmas. The compositions of the endmembers in each of the six mixing models in figure 9 were chosen in such a way to bracket the lowest and highest SiO_2 concentrations of both modeled melts, as well as to bracket the lowest and highest values of the measured Suswa melt inclusions. We mixed the chosen endmember composition melts together in 10% increments and show the trajectory of mixing between these endmember magmas on the major element composition of hybrid mixed magmas. The tick marks on the gray lines (fig 9) represent 10% increments of mixing. A seventh model was created to show a mixing path between the average composition of the high alkali Suswa melt inclusions and whole rock compositions that continues through to the Eburru inclusions and whole rock compositions. The slopes of these mixing models run orthogonally to the MELTs fractional crystallization models, and through the seventh mixing model we show that it is possible to create the otherwise puzzling array of magma compositions displayed by

Suswa and Eburru melt inclusions and whole rocks with a mixture of the magmas from the MELTs models discussed above.

These MELTs models and mixing calculations show that magma evolution in the thick continental lithosphere of Kenya is complex. The observed compositions of evolved, alkalic rocks in this portion of the East Africa Rift require multiple stages of crystallization, assimilation, and mixing between magmas that themselves have crystallized and assimilated to variable degrees. Our new direct measurements of H_2O and fO_2 of these evolved magmas (the only direct measurements yet produced, to our knowledge) demonstrate that these processes begin in the Central Peralkaline Province with magmas that are dry and reduced, and that the bulk of crystallization must proceed at low H_2O and fO_2. This suggests that the mantle source of magmas in the Central Peralkaline Province is itself dry and reduced, much like that of the depleted upper mantle that feeds the mid-ocean ridge spreading center system, and that neither fO_2 nor H_2O can play a large role in generating the nature of the geophysical anomaly observed under the Kenyan portion of the East African Rift. Whether the mantle sources of other lavas erupted to the north and south of the Central Peralkaline Province, and those of the Western Branch Rift are similarly dry and with low fO_2 is unknown and will require further constraints on the pre-eruptive H_2O contents of more magmas along the East African Rift.

Conclusions

The Suswa phonolites were formed through a complex combination of fractional crystallization and magma mixing. The MELTs models suggested by White et al., (2012) were not successful in reaching the lower SiO_2 melt inclusion compositions compared to whole rock measured in this study. In order to reach these higher alkali compositions, fractional crystallization had to have begun using an alkali basalt of higher alkali concentrations (Na_2O ~4.5 wt% and K_2O ~1.8 wt%) than was assumed by White et al. (2012). This model (i.e., one that starts at higher alkali contents) of fractional crystallization was successful in reaching the melt inclusion compositions of total alkalis and water but was unsuccessful in matching all the major elements of the measured inclusions. White et al., (2012) indicates the importance of magma mixing in the creation of the phonolitic Suswa compositions. We assessed this quantitatively by mixing MELTs model magma compositions from Suswa and Eburru. There is a negative slope between Suswa melt inclusion/whole rock compositions and Eburru melt inclusion/whole rock compositions that cannot be explained by simple crystal fractionation, but our mixing models demonstrates that mixtures between these two crystallization pathways can possibly create the magma compositions of highly evolved Suswa inclusions.

The Eburru trachytes were likely formed by the combination of fractional crystallization and crustal assimilation of the Pan African Lithosphere. A MELTs model of fractional crystallization of a low H_2O basalt (using the composition of ES12 of Elmenteita, White et al., 2012 as a starting composition) was able to replicate the compositions of Eburru melt inclusions for total alkalis and most of the major elements.

This model was unsuccessful in reaching the high H_2O compositions of the melt inclusions, indicating that water must have been brought in after substantial crystallization had generated a high SiO_2 magma. Using constraints produced by Scoggins (2022) that places constraints on the H_2O contents of the Pan African Lithosphere of 0-0.4 wt%, we were able to quantitatively assess the impact of crustal assimilation of hydrated Pan African Lithosphere into relatively dry, evolved Eburru magma. Broadly, small percents of mixtures of low degree melts of the Pan African Lithosphere are more likely as they lower the chances of significantly changing the values of the major element compositions. We find that 0.1% melts of a Pan African Lithosphere containing between 0.3-0.4 wt% H_2O contain between 23-31 wt% H_2O. To match the H_2O contents measured in Eburru inclusions requires between 8-21% of this hydrous melt of the Pan African lithosphere mixed into the dry evolved Eburru MELTs model compositions. In sum, we demonstrate that the alkaline magmas of the Central Kenya Peralkaline Province reflect complex series of crystallization, crustal assimilation, and magma mixing in the lithosphere (Fig 10), and that the mantle sources of these magmas may be dry and reduced.

References

Bastow, I. D., Nyblade, A. A., Stuart, G. W., Rooney, T. O., & Benoit, M. H. (2008). Upper mantle seismic structure beneath the Ethiopian hot spot: Rifting at the edge of the African low-velocity anomaly. *Geochemistry, Geophysics, Geosystems*, *9*(12).

Brounce, M., Stolper, E., & Eiler, J. (2022). The mantle source of basalts from Reunion Island is not more oxidized than the MORB source mantle. *Contributions to Mineralogy and Petrology*, *177*(1), 1-18.

Buck, W. R. (2004). 1. Consequences of asthenospheric variability on continental rifting. In *Rheology and deformation of the lithosphere at continental margins* (pp. 1-30). Columbia University Press.

Burgisser, A., Alletti, M., & Scaillet, B. (2015). Simulating the behavior of volatiles belonging to the C–O–H–S system in silicate melts under magmatic conditions with the software D-Compress. *Computers & Geosciences*, *79*, 1-14.

Clarke, M. C. (1990). *Geological, Volcanological and Hydrogeological Controls on the Occurrence of Geothermal Activity in the Area Surrounding Lake Naivasha, Kenya: With Coloured 1:250000 Geological Maps*. Ministry of Energy.

Condie, K. C., & Kröner, A. (2008). When did plate tectonics begin? Evidence from the geologic record. In *When did plate tectonics begin on planet Earth* (Vol. 440, pp. 281-294). Geological Society of America Special Papers.

Cottrell, E., Birner, S. K., Brounce, M., Davis, F. A., Waters, L. E., & Kelley, K. A. (2021). Oxygen fugacity across tectonic settings. *Magma Redox Geochemistry*, 33-61.

Dasgupta, R., & Hirschmann, M. M. (2007). Effect of variable carbonate concentration on the solidus of mantle peridotite. *American Mineralogist*, *92*(2-3), 370-379.

de Moor, J. M., Fischer, T. P., King, P. L., Botcharnikov, R. E., Hervig, R. L., Hilton, D. R., ... & Ramirez, C. (2013). Volatile-rich silicate melts from Oldoinyo Lengai volcano (Tanzania): Implications for carbonatite genesis and eruptive behavior. *Earth and Planetary Science Letters*, *361*, 379-390.

Dixon, J. E., Leist, L., Langmuir, C., & Schilling, J. G. (2002). Recycled dehydrated lithosphere observed in plume-influenced mid-ocean-ridge basalt. *Nature*, *420*(6914), 385-389.

Dixon, J. E., Stolper, E. M., & Holloway, J. R. (1995). An experimental study of water and carbon dioxide solubilities in mid-ocean ridge basaltic liquids. Part I: calibration and solubility models. *Journal of Petrology*, *36*(6), 1607-1631.

Dobrynina, A. A., Albaric, J., Deschamps, A., Perrot, J., Ferdinand, R. W., Déverchère, J., ... & Chechel’nitskii, V. V. (2017). Seismic wave attenuation in the lithosphere of the North Tanzanian divergence zone (East African rift system). *Russian Geology and Geophysics*, *58*(2), 253-265.

Donovan, A., Blundy, J., Oppenheimer, C., & Buisman, I. (2018). The 2011 eruption of Nabro volcano, Eritrea: perspectives on magmatic processes from melt inclusions. *Contributions to Mineralogy and Petrology*, *173*(1), 1-23.

Ebinger, C. J., Yemane, T., Woldegabriel, G., Aronson, J. L., & Walter, R. C. (1993). Late Eocene–Recent volcanism and faulting in the southern main Ethiopian rift. *Journal of the Geological Society*, *150*(1), 99-108.

Emry, E. L., Shen, Y., Nyblade, A. A., Flinders, A., & Bao, X. (2019). Upper mantle Earth structure in Africa from full‐wave ambient noise tomography. *Geochemistry, Geophysics, Geosystems*, *20*(1), 120-147.

Field, L., Barnie, T., Blundy, J., Brooker, R. A., Keir, D., Lewi, E., & Saunders, K. (2012). Integrated field, satellite and petrological observations of the November 2010 eruption of Erta Ale. *Bulletin of Volcanology*, *74*(10), 2251-2271.

Field, L., Blundy, J., Brooker, R. A., Wright, T., & Yirgu, G. (2012). Magma storage conditions beneath Dabbahu Volcano (Ethiopia) constrained by petrology, seismicity and satellite geodesy. *Bulletin of Volcanology*, *74*(5), 981-1004.

Forsyth, D., & Uyeda, S. (1975). On the relative importance of the driving forces of plate motion. *Geophysical Journal International*, *43*(1), 163-200.

George, R., & Rogers, N. (2002). Plume dynamics beneath the African plate inferred from the geochemistry of the Tertiary basalts of southern Ethiopia. *Contributions to Mineralogy and Petrology*, *144*(3), 286-304.

Gualda, G. A., & Ghiorso, M. S. (2015). MELTS_Excel: A Microsoft Excel‐based MELTS interface for research and teaching of magma properties and evolution. *Geochemistry, Geophysics, Geosystems*, *16*(1), 315-324.

Head, E. M., Shaw, A. M., Wallace, P. J., Sims, K. W., & Carn, S. A. (2011). Insight into volatile behavior at Nyamuragira volcano (DR Congo, Africa) through olivine‐hosted melt inclusions. *Geochemistry, Geophysics, Geosystems*, *12*(10).

Hirschmann, M. M., Tenner, T., Aubaud, C., & Withers, A. C. (2009). Dehydration melting of nominally anhydrous mantle: The primacy of partitioning. *Physics of the Earth and Planetary Interiors*, *176*(1-2), 54-68.

Jackson, I., & Faul, U. H. (2010). Grainsize-sensitive viscoelastic relaxation in olivine: Towards a robust laboratory-based model for seismological application. *Physics of the Earth and Planetary Interiors*, *183*(1-2), 151-163.

Jenner, F. E., & O'Neill, H. S. C. (2012). Analysis of 60 elements in 616 ocean floor basaltic glasses. *Geochemistry, Geophysics, Geosystems*, *13*(2).

Jugo, P. J., Wilke, M., & Botcharnikov, R. E. (2010). Sulfur K-edge XANES analysis of natural and synthetic basaltic glasses: Implications for S speciation and S content as function of oxygen fugacity. *Geochimica et Cosmochimica Acta*, *74*(20), 5926-5938.

Karato, S. I., & Jung, H. (2003). Effects of pressure on high-temperature dislocation creep in olivine. *Philosophical Magazine*, *83*(3), 401-414.

Klimm, K., Kohn, S. C., & Botcharnikov, R. E. (2012). The dissolution mechanism of sulphur in hydrous silicate melts. II: Solubility and speciation of sulphur in hydrous silicate melts as a function of fO_2. *Chemical Geology*, *322*, 250-267.

Kogiso, T., Hirschmann, M. M., & Pertermann, M. (2004). High-pressure partial melting of mafic lithologies in the mantle. *Journal of Petrology*, *45*(12), 2407-2422.

Kress, V. C., & Carmichael, I. S. (1991). The compressibility of silicate liquids containing Fe_2O_3 and the effect of composition, temperature, oxygen fugacity and pressure on their redox states. *Contributions to Mineralogy and Petrology*, *108*(1), 82-92.

Muth, M. J., & Wallace, P. J. (2021). Slab-derived sulfate generates oxidized basaltic magmas in the southern Cascade arc (California, USA). *Geology*, *49*(10), 1177-1181.

Newman, S., & Lowenstern, J. B. (2002). VolatileCalc: a silicate melt–H2O–CO2 solution model written in Visual Basic for excel. *Computers & Geosciences*, *28*(5), 597-604.

Nicklas, R. W., Hahn, R. K. M., & Day, J. M. D. (2022). Oxidation of La Reunion lavas with MORB-like fO_2 by assimilation. *GEOCHEMICAL PERSPECTIVES LETTERS*, *20*, 32-36.

Pasyanos, M. E., 2010. Lithospheric thickness modeled from long-period surface wave dispersion, Tectonophysics, vol 481, Issues 1–4, 38-50.

Ravel, B., & Newville, M.A.T.H.E.N.A. (2005). ATHENA, ARTEMIS, HEPHAESTUS: data analysis for X-ray absorption spectroscopy using IFEFFIT. *Journal of synchrotron radiation*, *12*(4), 537-541.

Ren, M., Omenda, P. A., Anthony, E. Y., White, J. C., Macdonald, R., & Bailey, D. K. (2006). Application of the QUILF thermobarometer to the peralkaline trachytes and pantellerites of the Eburru volcanic complex, East African Rift, Kenya. *Lithos*, *91*(1-4), 109-124.

Rooney, T. O., Herzberg, C., & Bastow, I. D. (2012). Elevated mantle temperature beneath East Africa. *Geology*, *40*(1), 27-30.

Schaeffer, A. J., & Lebedev, S. (2013). Global shear speed structure of the upper mantle and transition zone. *Geophysical Journal International*, *194*(1), 417-449.

Schilling, J. G., Kingsley, R. H., Hanan, B. B., & McCully, B. L. (1992). Nd-Sr-Pb isotopic variations along the Gulf of Aden: Evidence for Afar mantle plume-continental lithosphere interaction. *Journal of Geophysical Research: Solid Earth*, *97*(B7), 10927-10966.

Scoggins, S. L. (2022). Pre-Erupted Water Concentrations in Erta Ale Lavas and Gulf of Aden Glasses and the Role of Water in Continental Rifting [Unpublished thesis]. University of California Riverside.

White, J. C., Espejel-García, V. V., Anthony, E. Y., & Omenda, P. (2012). Open system evolution of peralkaline trachyte and phonolite from the Suswa volcano, Kenya rift. *Lithos*, *152*, 84-104.

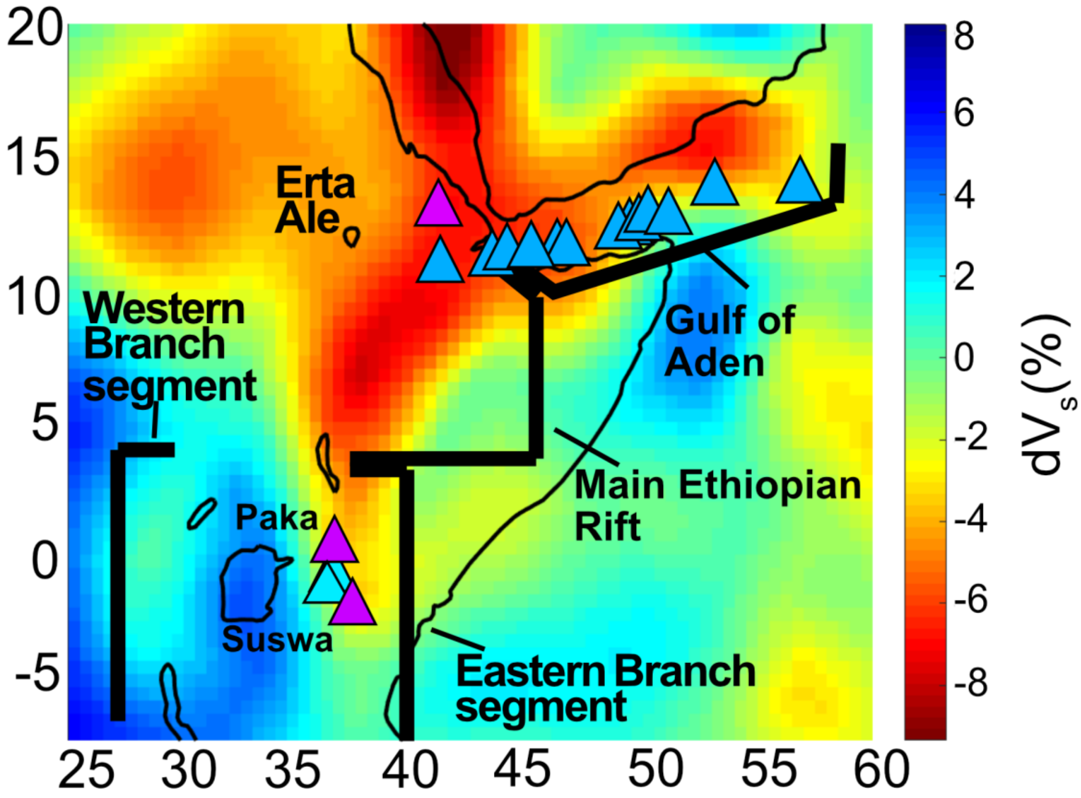

Figure 1: A tomographic model (Schaeffer and Lebedev, 2013) of the East African Rift region with volcanics superimposed. The purple triangles correspond to Suswa, Paka and Erta Ale volcanoes. The blue triangles represent other volcanic regions in the Central Peralkaline Province (light blue), as well as submarine glasses in the Gulf of Aden (dark blue).

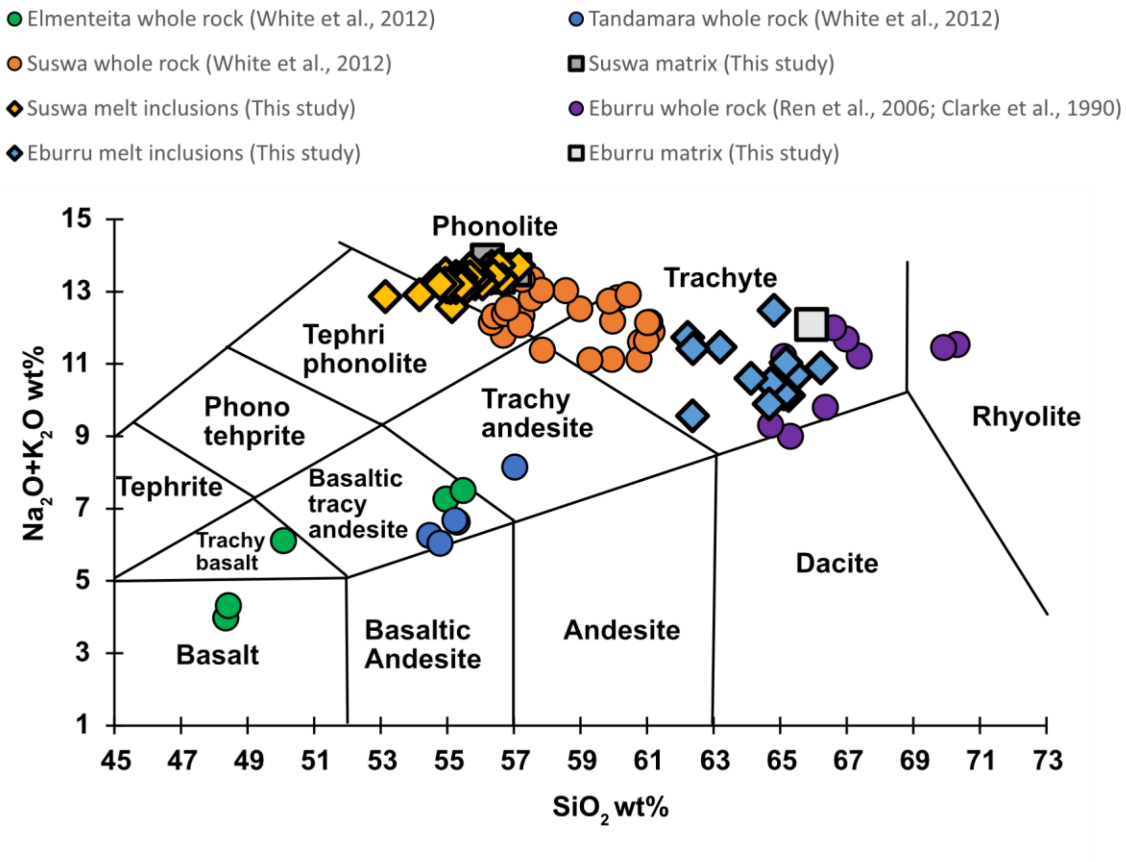

Figure 2: Total alkali plot of samples from this study (inclusions and matrices) and whole rock data for Suswa, Eburru, Elmenteita and Tandamara (White et al., 2012; Ren et al., 2006; Clarke et al., 1990) with rock compositions labeled.

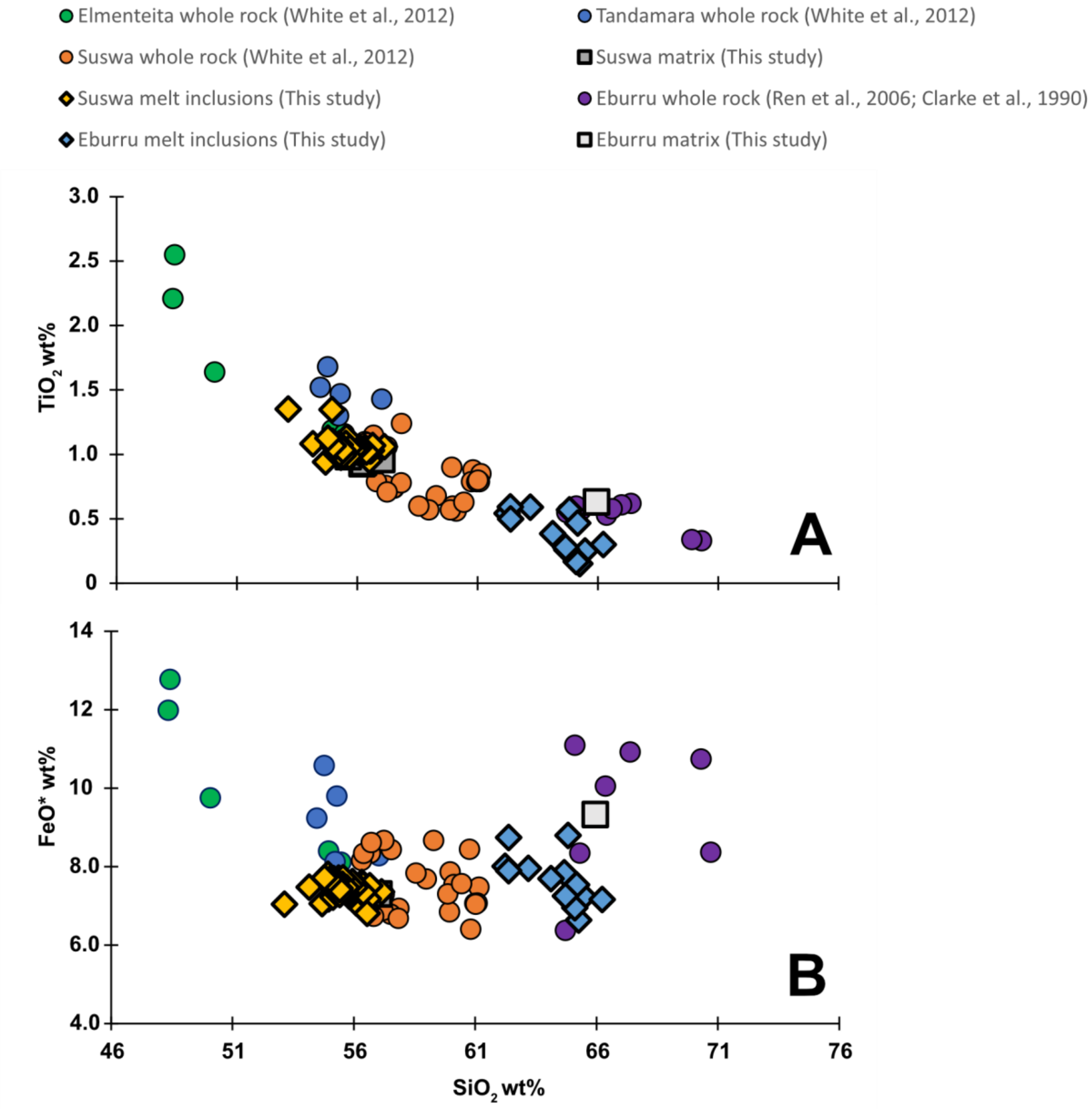

Figure 3: A model of TiO_2 vs SiO_2 (A) and FeO* vs SiO_2 plots for Suswa and Eburru samples compared to Suswa, Eburru, Elmenteita and Tandamara whole rock (White et al., 2012; Ren et al., 2006; Clarke et al., 1990).

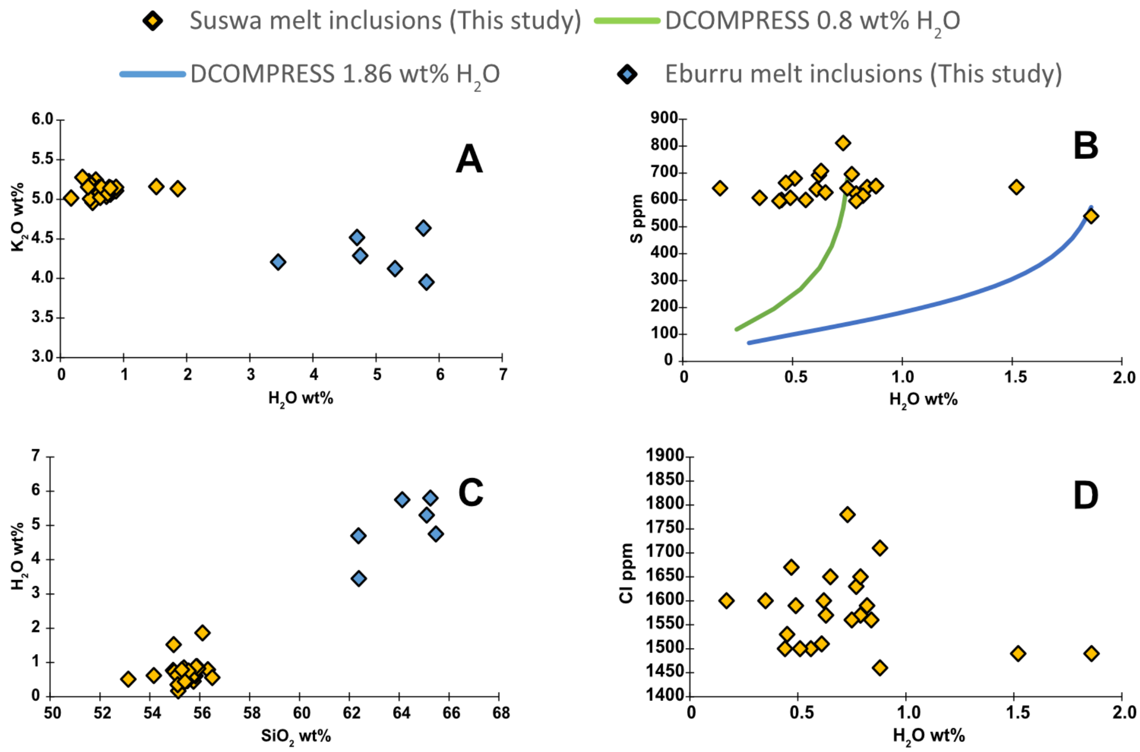

Figure 4: A model of H_2O vs K_2O (A), S (B), SiO_2 (C) and Cl (D) plots for Eburru and Suswa melt inclusions in this study. For model (B) degassing lines are present, measured using DCOMPRESS of (Burgisser et al., 2015; see the discussion section for more information).

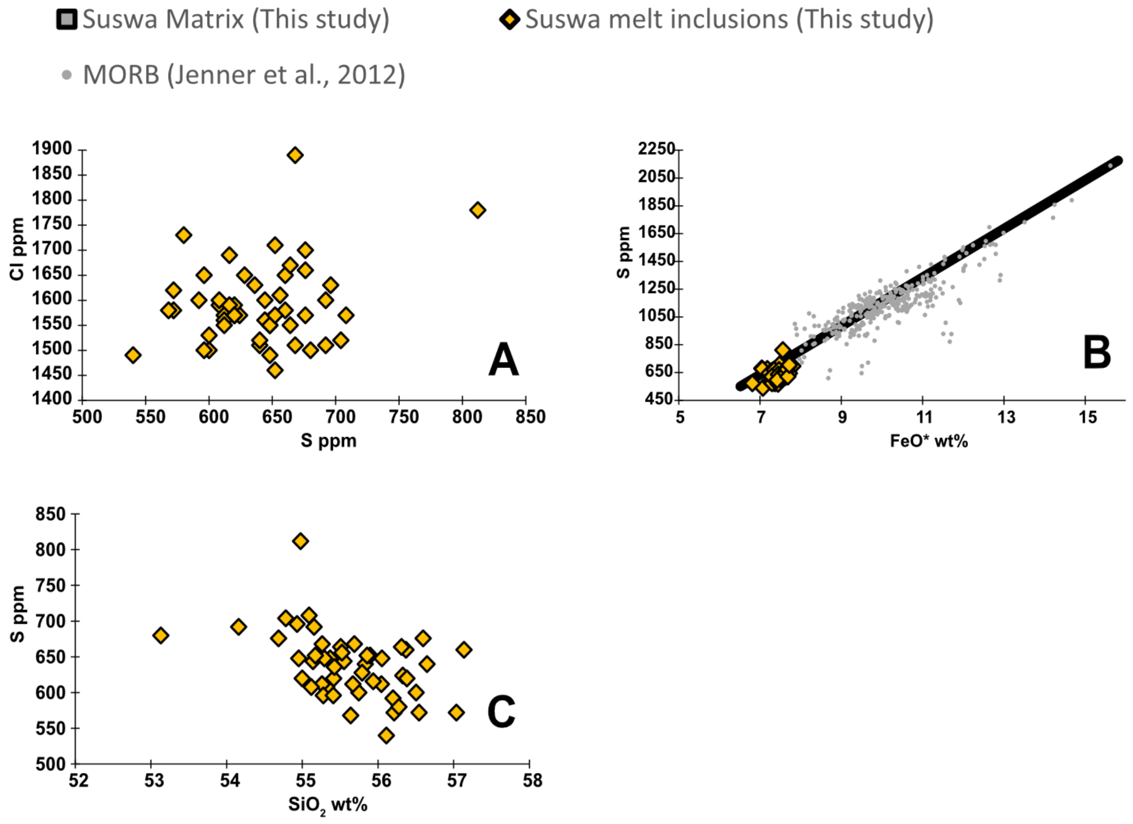

Figure 5: A model of S vs Cl (A), FeO* (B) and SiO_2 (C) plots for Suswa melt inclusions in this study. For model (B), melt inclusions are compared to MORB data from Jenner et al., (2012) and lie on/underneath the empirical line defined by MORB of the sulfur content at sulfide saturation (Jenner et al., 2012).

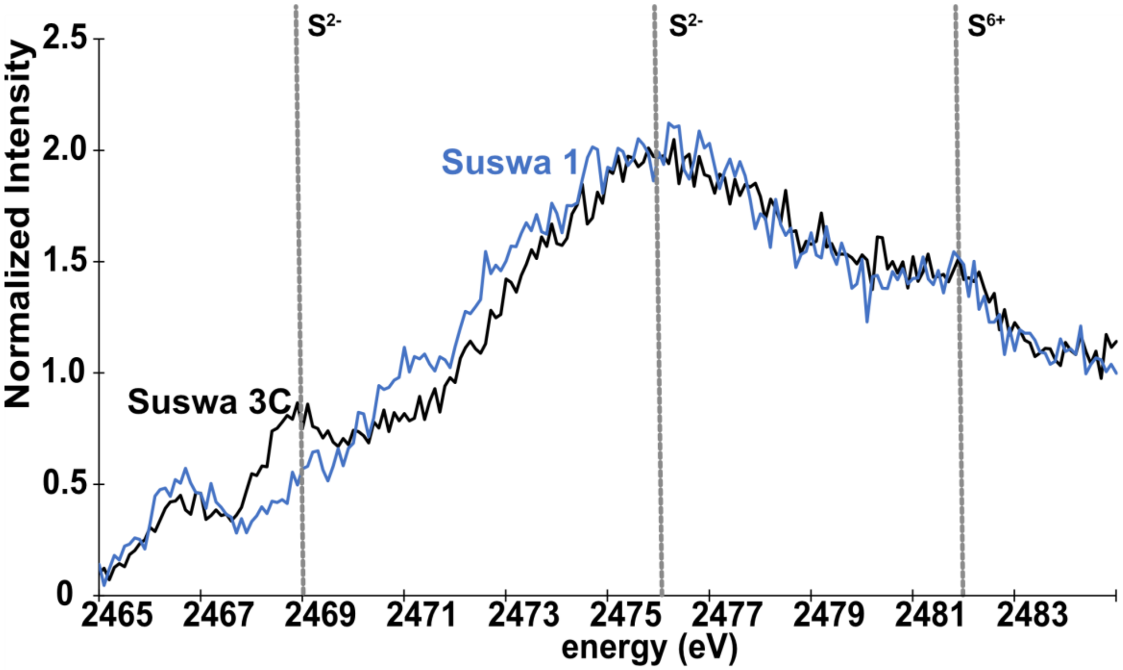

Figure 6: A model of XANES spectra of Suswa samples 1 (blue) and 3C (black) with lines superimposed over the apparent peaks for S^{2-} and S^{6+}.

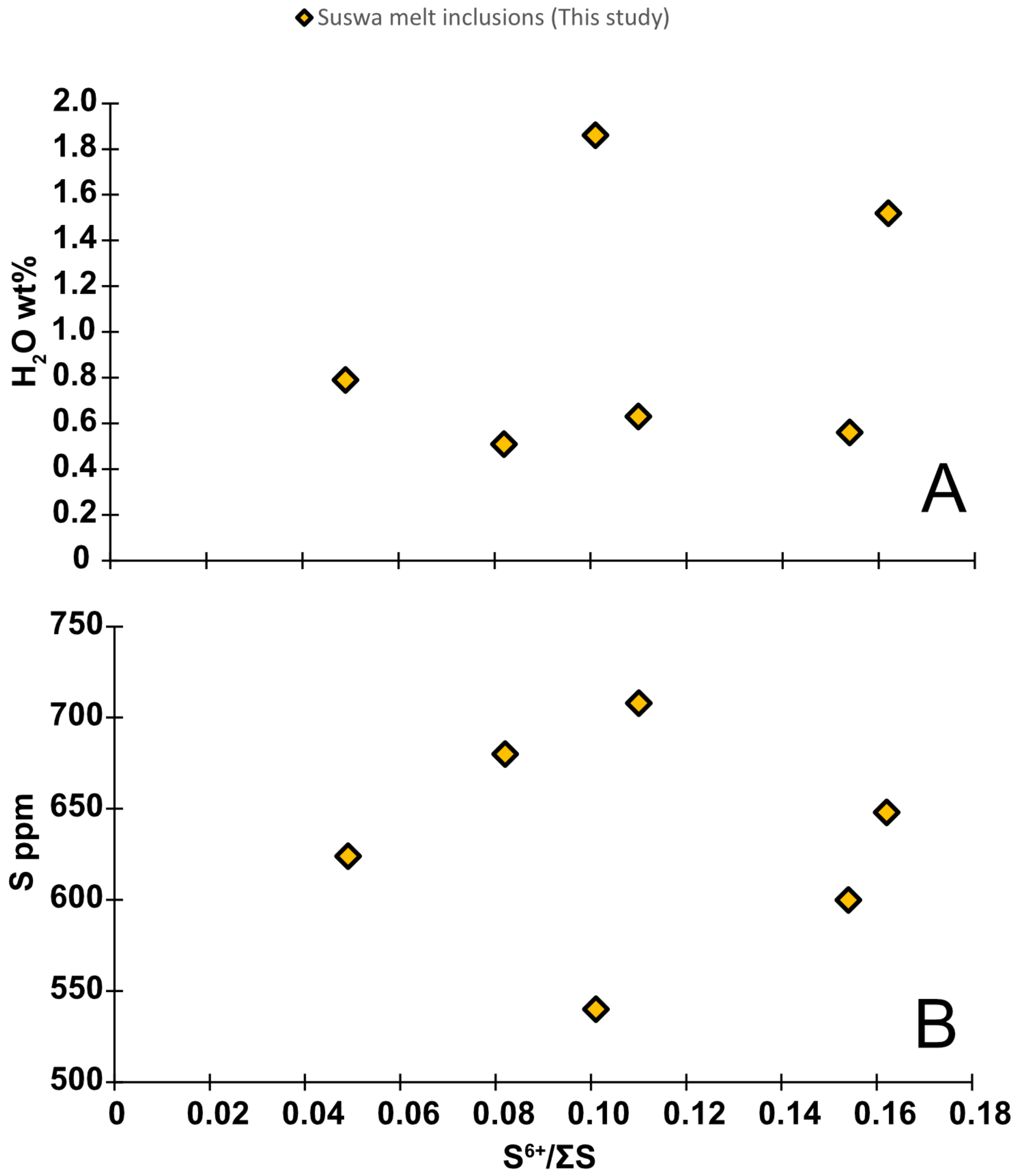

Figure 7: A model of $S^{6+}/\sum S$ vs H_2O (A) and S (B) of Suswa melt inclusions from this study.

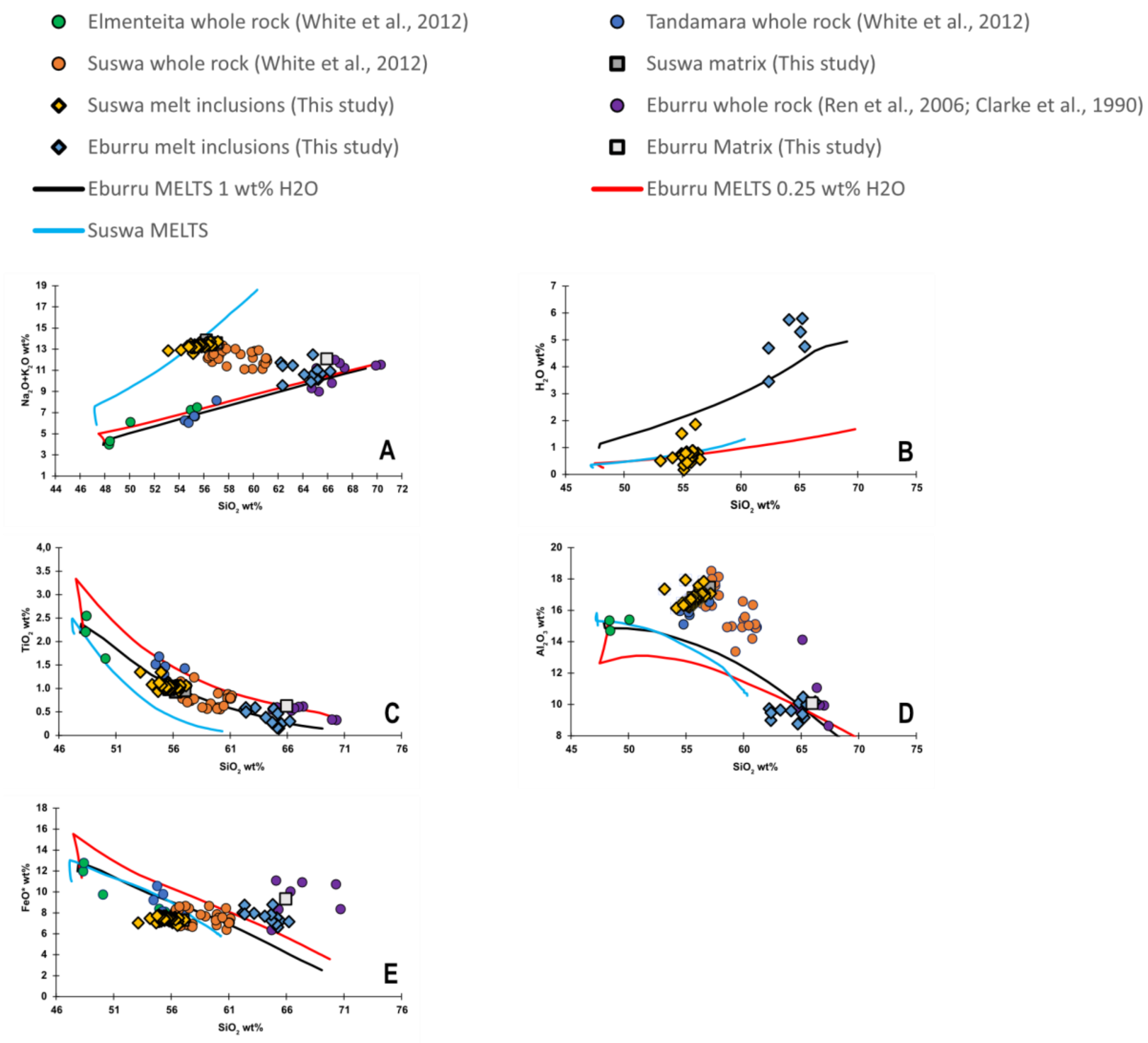

Figure 8: MELTs models of Suswa (blue line) and Eburru (red and black lines) showing the crystallization conditions of our measured samples.

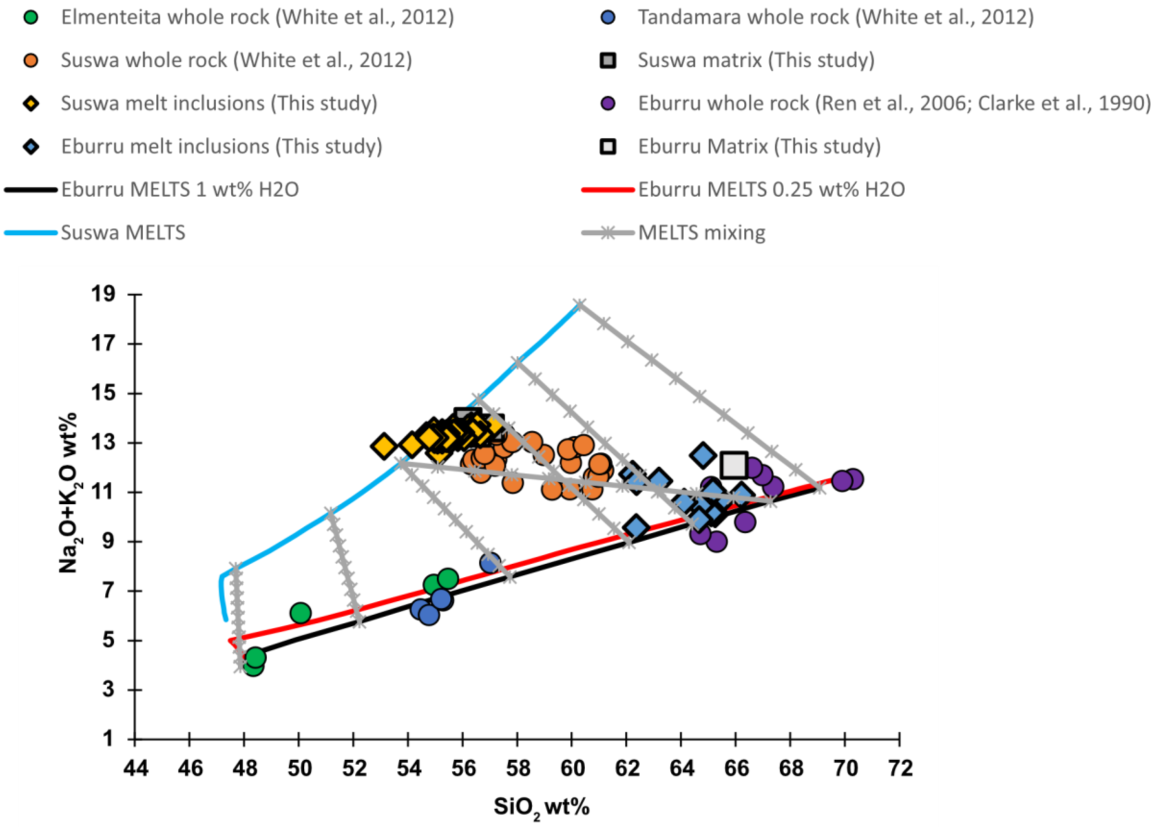

Figure 9: A model of magma mixing between compositions of MELTs models of Suswa (blue line) and Eburru (red and black lines) on the total alkali plot of Figure 2.

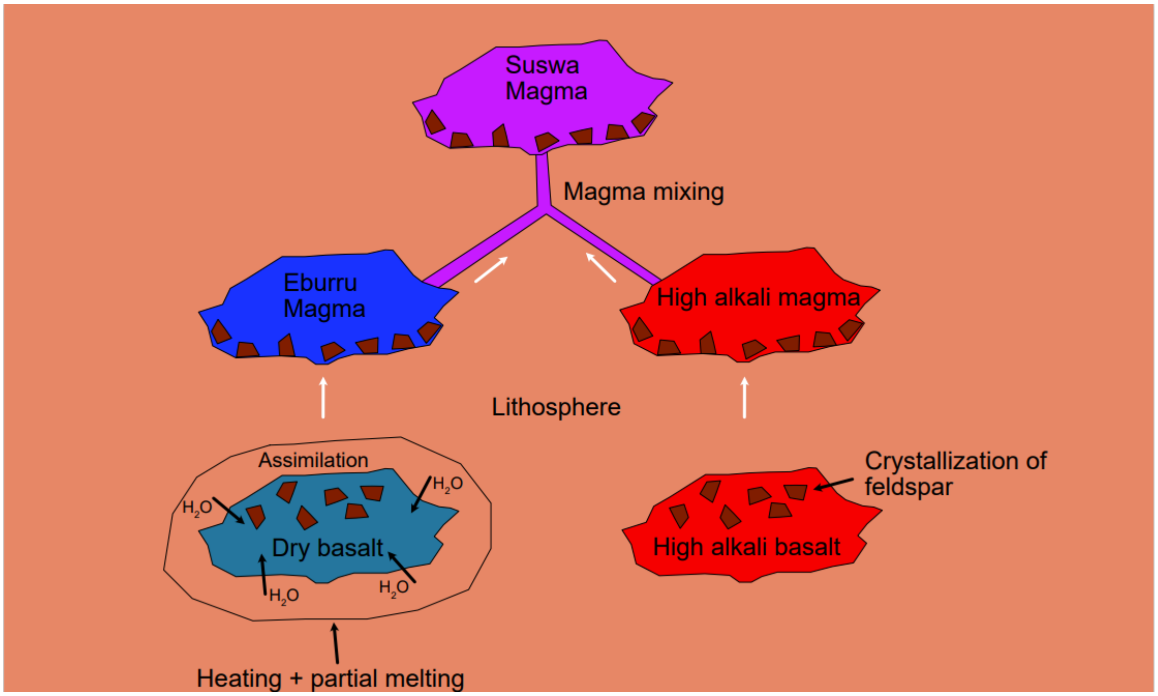

Figure 10: An illustration to show how the processes of fractional crystallization, crustal assimilation and magma mixing between two dry basalts of differing compositions can work in combination to create the widely varied evolved magmas of Suswa and Eburru in the Central Peralkaline Province.

Table 1

Suswa major elements

Sample		Suswa-01A	Suswa-01B	Suswa-02A	Suswa-02B	Suswa-03A
SiO_2	(wt%)	56.33	56.50	55.37	55.75	54.95
TiO_2	(wt%)	1.05	0.95	1.07	1.04	1.35
Al_2O_3	(wt%)	17.22	17.16	16.67	16.80	17.94
FeO*	(wt%)	7.59	7.29	7.71	7.33	7.18
MgO	(wt%)	0.67	0.60	0.67	0.66	0.67
MnO	(wt%)	0.32	0.30	0.30	0.29	0.30
CaO	(wt%)	1.92	1.84	2.01	1.96	1.97
Na_2O	(wt%)	8.63	8.38	8.19	8.14	8.34
K_2O	(wt%)	5.07	5.24	5.11	5.22	5.16
P_2O_5	(wt%)	0.19	0.18	0.23	0.17	0.18
S	(ppm)	624	600	648	600	648
Cl	(ppm)	1570	1500	1560	1530	1490
H_2O	(wt%)	0.79	0.56		0.84	0.45

Table 1 Cont.

Suswa major elements

Sample		Suswa-03B	Suswa-03C	Suswa-04A	Suswa-04B	Suswa-05A
SiO_2	(wt%)	53.13	56.11	54.93	55.32	56.37
TiO_2	(wt%)	1.35	1.05	1.08	0.98	1.04
Al_2O_3	(wt%)	17.36	17.58	16.48	16.45	16.91
FeO*	(wt%)	7.04	7.07	7.81	7.57	7.55
MgO	(wt%)	0.64	0.65	0.69	0.67	0.70
MnO	(wt%)	0.30	0.32	0.33	0.34	0.31
CaO	(wt%)	3.63	1.95	1.95	2.01	1.97
Na_2O	(wt%)	7.91	8.30	8.09	7.98	8.39
K_2O	(wt%)	4.96	5.14	5.15	5.18	5.10
P_2O_5	(wt%)	1.75	0.17	0.23	0.22	0.21
S	(ppm)	680	540	696	608	660
Cl	(ppm)	1500	1490	1630	1590	1580
H_2O	(wt%)	1.52	0.51	1.86	0.77	0.49

Table 1 Cont.
Suswa major elements

Sample		Suswa-05B	Suswa-06A	Suswa-07A	Suswa-07B	Suswa-07C
SiO_2	(wt%)	56.20	56.04	56.31	57.14	56.59
TiO_2	(wt%)	1.01	1.01	1.04	1.06	1.03
Al_2O_3	(wt%)	17.00	16.88	16.89	17.07	17.10
FeO*	(wt%)	7.49	7.46	7.35	7.35	7.18
MgO	(wt%)	0.69	0.66	0.68	0.68	0.68
MnO	(wt%)	0.32	0.31	0.30	0.33	0.31
CaO	(wt%)	1.92	2.01	1.95	2.00	1.98
Na_2O	(wt%)	8.55	8.23	8.40	8.52	8.36
K_2O	(wt%)	5.06	5.19	4.98	5.21	5.05
P_2O_5	(wt%)	0.23	0.24	0.18	0.23	0.21
S	(ppm)	592	612	664	660	676
Cl	(ppm)	1600	1570	1550	1650	1700
H_2O	(wt%)					

Table 1 Cont.

Suswa major elements

Sample		Suswa-08A	Suswa-08B	Suswa-09A	Suswa-09B	Suswa-10A
SiO_2	(wt%)	55.83	55.51	55.90	54.69	
TiO_2	(wt%)	1.01	1.08	1.02	0.94	
Al_2O_3	(wt%)	16.52	16.55	16.69	16.47	
FeO*	(wt%)	7.24	7.49	7.48	7.06	
MgO	(wt%)	0.67	0.69	0.66	0.64	
MnO	(wt%)	0.29	0.31	0.29	0.30	
CaO	(wt%)	1.97	1.97	1.94	2.00	
Na_2O	(wt%)	8.07	8.18	8.23	8.01	
K_2O	(wt%)	5.15	5.01	5.11	5.29	
P_2O_5	(wt%)	0.20	0.22	0.20	0.18	
S	(ppm)	640	664	652	676	676
Cl	(ppm)	1510	1670	1710	1570	1660
H_2O	(wt%)			0.61	0.47	

Table 1 Cont.

Suswa major elements

Sample		Suswa-10B	Suswa-11A	Suswa-11B	Suswa-11C	Suswa-12A
SiO_2	(wt%)	55.14	54.98	54.16	55.09	55.79
TiO_2	(wt%)	1.00	1.10	1.08	1.05	0.99
Al_2O_3	(wt%)	16.40	16.34	16.14	16.38	16.78
FeO*	(wt%)	7.22	7.56	7.48	7.48	7.30
MgO	(wt%)	0.61	0.68	0.74	0.72	0.67
MnO	(wt%)	0.30	0.31	0.29	0.32	0.30
CaO	(wt%)	1.92	2.05	2.01	2.00	1.98
Na_2O	(wt%)	7.58	8.09	7.84	8.09	8.15
K_2O	(wt%)	5.02	5.04	5.08	5.03	5.16
P_2O_5	(wt%)	0.20	0.26	0.25	0.23	0.16
S	(ppm)	644	812	692	708	628
Cl	(ppm)	1600	1780	1600	1570	1650
H_2O	(wt%)	0.88			0.17	0.73

Table 1 Cont.

Suswa major elements

Sample		Suswa-12B	Suswa-13A	Suswa-13B	Suswa-13C	Suswa-13D
SiO_2	(wt%)	55.26	56.54	56.65	56.38	
TiO_2	(wt%)	1.08	1.03	1.07	1.02	
Al_2O_3	(wt%)	16.34	17.83	16.92	17.06	
FeO*	(wt%)	7.35	6.81	7.52	7.34	
MgO	(wt%)	0.69	0.70	0.69	0.69	
MnO	(wt%)	0.32	0.27	0.33	0.29	
CaO	(wt%)	2.03	1.91	1.99	1.98	
Na_2O	(wt%)	8.23	8.56	8.39	8.49	
K_2O	(wt%)	5.19	5.18	4.95	4.96	
P_2O_5	(wt%)	0.23	0.23	0.22	0.17	
S	(ppm)	668	572	640	620	616
Cl	(ppm)	1890	1260	1520	1590	1690
H_2O	(wt%)	0.62	0.63	0.65		

Table 1 Cont.

Suswa major elements

Sample		Suswa-13E	Suswa-14A	Suswa-14B	Suswa-14C	Suswa-15A
SiO_2	(wt%)	56.05	55.94	55.86	55.55	55.67
TiO_2	(wt%)	1.05	1.05	1.03	1.13	0.98
Al_2O_3	(wt%)	16.73	16.80	16.77	16.44	16.90
FeO*	(wt%)	7.48	7.62	7.53	7.72	7.34
MgO	(wt%)	0.72	0.67	0.70	0.71	0.62
MnO	(wt%)	0.31	0.32	0.31	0.31	0.32
CaO	(wt%)	1.99	1.98	1.97	2.07	1.92
Na_2O	(wt%)	8.10	8.29	8.21	8.04	8.34
K_2O	(wt%)	5.12	5.13	5.15	5.08	5.30
P_2O_5	(wt%)	0.22	0.20	0.21	0.20	0.19
S	(ppm)	648	616	652	644	612
Cl	(ppm)	1550	1590	1460	1560	1560
H_2O	(wt%)		0.82	0.88	0.75	

Table 1 Cont.

Suswa major elements

Sample		Suswa-15B	Suswa-15C	Suswa-16A	Suswa-16B	Suswa-16C
SiO_2	(wt%)	55.52	55.69	55.29	55.41	55.26
TiO_2	(wt%)	1.08	1.05	1.07	1.01	1.06
Al_2O_3	(wt%)	16.73	16.64	16.21	16.61	16.47
FeO*	(wt%)	7.55	7.47	7.63	7.29	7.51
MgO	(wt%)	0.71	0.70	0.68	0.64	0.65
MnO	(wt%)	0.32	0.30	0.30	0.32	0.31
CaO	(wt%)	2.08	2.04	2.00	1.90	2.00
Na_2O	(wt%)	8.30	8.25	8.04	8.05	7.98
K_2O	(wt%)	5.14	5.17	5.19	5.33	5.13
P_2O_5	(wt%)	0.22	0.23	0.19	0.21	0.19
S	(ppm)	656	668	648	620	612
Cl	(ppm)	1610	1510	1550	1570	1550
H_2O	(wt%)					

Table 1 Cont.

Suswa major elements

Sample		Suswa-16D	Suswa-16E	Suswa-16F	Suswa-17A	Suswa-17B
SiO_2	(wt%)	55.15	55.42	55.17	55.28	55.12
TiO_2	(wt%)	1.07	0.99	1.06	1.01	1.06
Al_2O_3	(wt%)	16.27	16.56	16.58	16.63	16.50
FeO*	(wt%)	7.70	7.45	7.59	7.52	7.51
MgO	(wt%)	0.69	0.64	0.67	0.65	0.71
MnO	(wt%)	0.32	0.32	0.32	0.33	0.31
CaO	(wt%)	1.98	1.91	1.93	1.95	2.00
Na_2O	(wt%)	8.05	8.04	8.06	8.12	7.99
K_2O	(wt%)	5.21	5.20	5.11	5.14	5.28
P_2O_5	(wt%)	0.23	0.19	0.24	0.21	0.22
S	(ppm)	692	636	652	596	608
Cl	(ppm)	1510	1630	1570	1650	1600
H_2O	(wt%)					0.79

Table 1 Cont.

Suswa major elements

Sample		Suswa-17C	Suswa-17D	Suswa-17E	Suswa-01 matrix	Suswa-05 matrix
SiO_2	(wt%)	55.41	55.00	54.78	56.21	56.55
TiO_2	(wt%)	1.03	1.07	1.13	0.92	0.95
Al_2O_3	(wt%)	16.70	16.35	16.32	17.23	17.31
FeO*	(wt%)	7.42	7.68	7.72	7.36	7.24
MgO	(wt%)	0.68	0.70	0.72	0.63	0.62
MnO	(wt%)	0.33	0.32	0.32	0.33	0.30
CaO	(wt%)	1.96	2.01	1.99	1.77	1.71
Na_2O	(wt%)	8.02	8.05	8.13	8.50	8.11
K_2O	(wt%)	5.16	5.17	5.09	5.36	5.27
P_2O_5	(wt%)	0.24	0.24	0.30	0.17	0.17
S	(ppm)	596	620	704	572	
Cl	(ppm)	1500	1570	1520	1620	
H_2O	(wt%)	0.35	0.44			

Table 1 Cont.

Suswa major elements

Sample		Suswa-08 matrix	Suswa-13 matrix	Suswa-16 matrix
SiO_2	(wt%)	56.28	57.03	55.64
TiO_2	(wt%)	0.93	0.96	0.98
Al_2O_3	(wt%)	16.93	17.46	16.79
FeO*	(wt%)	7.27	7.30	7.44
MgO	(wt%)	0.59	0.62	0.59
MnO	(wt%)	0.29	0.31	0.31
CaO	(wt%)	1.83	1.81	1.81
Na_2O	(wt%)	8.30	8.39	8.10
K_2O	(wt%)	5.13	5.21	5.19
P_2O_5	(wt%)	0.19	0.17	0.19
S	(ppm)	580	572	568
Cl	(ppm)	1730	1580	1580
H_2O	(wt%)			

*Total Fe content reported as FeO

Table 2

Suswa host compositions

Sample		Suswa-01A	Suswa-01B	Suswa-02A	Suswa-02B	Suswa-03A
SiO_2	(wt%)	63.44	63.44	62.65	62.65	62.40
TiO_2	(wt%)	0.12	0.12	0.09	0.09	0.11
Al_2O_3	(wt%)	19.97	19.97	19.55	19.55	21.58
FeO	(wt%)	0.13	0.13	0.15	0.15	0.19
CaO	(wt%)	1.24	1.24	1.22	1.22	2.77
Na_2O	(wt%)	7.68	7.68	7.75	7.75	7.88
K_2O	(wt%)	4.87	4.87	4.82	4.82	3.13

Table 2 Cont.

Suswa host compositions

Sample		Suswa-03B	Suswa-03C	Suswa-04A	Suswa-04B	Suswa-05A
SiO_2	(wt%)	62.40	62.40	65.39	65.39	63.92
TiO_2	(wt%)	0.11	0.11	0.12	0.12	0.10
Al_2O_3	(wt%)	21.58	21.58	20.53	20.53	19.74
FeO	(wt%)	0.19	0.19	0.20	0.20	0.19
CaO	(wt%)	2.77	2.77	1.27	1.27	0.98
Na_2O	(wt%)	7.88	7.88	7.93	7.93	7.52
K_2O	(wt%)	3.13	3.13	4.75	4.75	5.27

Table 2 Cont.

Suswa host compositions

Sample		Suswa-05B	Suswa-06A	Suswa-07A	Suswa-07B	Suswa-07C
SiO_2	(wt%)	63.92	64.64	64.73	64.73	64.73
TiO_2	(wt%)	0.10	0.12	0.13	0.13	0.13
Al_2O_3	(wt%)	19.74	20.16	20.85	20.85	20.85
FeO	(wt%)	0.19	0.19	0.17	0.17	0.17
CaO	(wt%)	0.98	1.14	1.41	1.41	1.41
Na_2O	(wt%)	7.52	7.75	8.08	8.08	8.08
K_2O	(wt%)	5.27	5.02	4.70	4.70	4.70

Table 2 Cont.

Suswa host compositions

Sample		Suswa-08A	Suswa-08B	Suswa-09A	Suswa-09B	Suswa-10A
SiO_2	(wt%)	64.35	64.35	63.93	63.93	65.43
TiO_2	(wt%)	0.08	0.08	0.09	0.09	0.13
Al_2O_3	(wt%)	20.08	20.08	19.78	19.78	20.50
FeO	(wt%)	0.19	0.19	0.19	0.19	0.20
CaO	(wt%)	1.14	1.14	1.17	1.17	1.27
Na_2O	(wt%)	7.69	7.69	7.73	7.73	7.79
K_2O	(wt%)	5.14	5.14	4.89	4.89	4.73

Table 2 Cont.

Suswa host compositions

Sample		Suswa-10B	Suswa-11A	Suswa-11B	Suswa-11C	Suswa-12A
SiO_2	(wt%)	65.43	64.33	64.33	64.33	64.26
TiO_2	(wt%)	0.13	0.07	0.07	0.07	0.11
Al_2O_3	(wt%)	20.50	20.16	20.16	20.16	20.08
FeO	(wt%)	0.20	0.18	0.18	0.18	0.19
CaO	(wt%)	1.27	1.23	1.23	1.23	1.19
Na_2O	(wt%)	7.79	7.60	7.60	7.60	7.58
K_2O	(wt%)	4.73	4.84	4.84	4.84	4.98

Table 2 Cont.

Suswa host compositions

Sample		Suswa-12B	Suswa-13A	Suswa-13B	Suswa-13C	Suswa-13D
SiO_2	(wt%)	64.26	64.74	64.74	64.74	64.74
TiO_2	(wt%)	0.11	0.13	0.13	0.13	0.13
Al_2O_3	(wt%)	20.08	20.51	20.51	20.51	20.51
FeO	(wt%)	0.19	0.17	0.17	0.17	0.17
CaO	(wt%)	1.19	1.15	1.15	1.15	1.15
Na_2O	(wt%)	7.58	7.64	7.64	7.64	7.64
K_2O	(wt%)	4.98	5.04	5.04	5.04	5.04

Table 2 Cont.

Suswa host compositions

Sample		Suswa-13E	Suswa-14A	Suswa-14B	Suswa-14C	Suswa-15A
SiO_2	(wt%)	64.74	63.22	63.22	63.22	63.07
TiO_2	(wt%)	0.13	0.08	0.08	0.08	0.09
Al_2O_3	(wt%)	20.51	20.11	20.11	20.11	19.78
FeO	(wt%)	0.17	0.16	0.16	0.16	0.18
CaO	(wt%)	1.15	1.39	1.39	1.39	1.14
Na_2O	(wt%)	7.64	7.66	7.66	7.66	7.37
K_2O	(wt%)	5.04	4.56	4.56	4.56	4.94

Table 2 Cont.

Suswa host compositions

Sample		Suswa-15B	Suswa-15C	Suswa-16A	Suswa-16B	Suswa-16C
SiO_2	(wt%)	63.07	63.07	63.54	63.54	63.54
TiO_2	(wt%)	0.09	0.09	0.09	0.09	0.09
Al_2O_3	(wt%)	19.78	19.78	20.00	20.00	20.00
FeO	(wt%)	0.18	0.18	0.17	0.17	0.17
CaO	(wt%)	1.14	1.14	1.16	1.16	1.16
Na_2O	(wt%)	7.37	7.37	7.29	7.29	7.29
K_2O	(wt%)	4.94	4.94	4.96	4.96	4.96

Table 2 Cont.

Suswa host compositions

Sample		Suswa-16D	Suswa-16E	Suswa-16F	Suswa-17A	Suswa-17B
SiO_2	(wt%)	63.54	63.54	63.54	58.68	58.68
TiO_2	(wt%)	0.09	0.09	0.09	0.11	0.11
Al_2O_3	(wt%)	20.00	20.00	20.00	18.32	18.32
FeO	(wt%)	0.17	0.17	0.17	0.19	0.19
CaO	(wt%)	1.16	1.16	1.16	1.20	1.20
Na_2O	(wt%)	7.29	7.29	7.29	7.34	7.34
K_2O	(wt%)	4.96	4.96	4.96	4.87	4.87

Table 2 Cont.

Suswa host compositions

Sample		Suswa-17C	Suswa-17D	Suswa-17E
SiO_2	(wt%)	58.68	58.68	58.68
TiO_2	(wt%)	0.11	0.11	0.11
Al_2O_3	(wt%)	18.32	18.32	18.32
FeO	(wt%)	0.19	0.19	0.19
CaO	(wt%)	1.20	1.20	1.20
Na_2O	(wt%)	7.34	7.34	7.34
K_2O	(wt%)	4.87	4.87	4.87

Table 3
Eburru major elements

Sample		Eb-01	Eb-03A	Eb-03B	Eb-04	Eb-05A
SiO_2	(wt%)	64.82	63.19	62.22	65.47	66.22
TiO_2	(wt%)	0.57	0.59	0.54	0.25	0.30
Al_2O_3	(wt%)	10.11	9.65	9.73	10.00	10.17
FeO*	(wt%)	8.80	7.96	8.01	7.24	7.16
MgO	(wt%)	0.02	0.00	0.02	0.01	0.01
MnO	(wt%)	0.26	0.23	0.24	0.22	0.22
CaO	(wt%)	0.52	0.48	0.49	0.25	0.32
Na_2O	(wt%)	7.88	7.27	7.63	6.40	6.53
K_2O	(wt%)	4.61	4.20	4.10	4.29	4.37
P_2O_5	(wt%)	0.04		0.03	0.05	0.03
H_2O	(wt%)				4.75	

Table 3 Cont.

Eburru major elements

Sample		Eb-05B	Eb-06	Eb-07A	Eb-07B	Eb-08A
SiO_2	(wt%)	65.17	62.37	65.25	65.10	64.71
TiO_2	(wt%)	0.47	0.59	0.15	0.17	0.26
Al_2O_3	(wt%)	10.47	8.99	9.17	9.37	8.77
FeO*	(wt%)	7.54	8.74	6.64	6.95	7.25
MgO	(wt%)	0.00	0.01	0.01	0.02	0.01
MnO	(wt%)	0.22	0.24	0.17	0.24	0.22
CaO	(wt%)	0.40	0.54	0.21	0.24	0.24
Na_2O	(wt%)	6.75	5.06	6.18	6.05	6.67
K_2O	(wt%)	4.29	4.52	3.95	4.12	3.81
P_2O_5	(wt%)	0.09	0.04	0.07	0.06	0.03
H_2O	(wt%)		4.70	5.80	5.30	

Table 3 Cont.
Eburru major elements

Sample		Eb-08B	Eb-09	Eb-10	Eb-05 matrix
SiO_2	(wt%)	64.67	64.12	62.38	65.96
TiO_2	(wt%)	0.28	0.38	0.50	0.63
Al_2O_3	(wt%)	7.84	9.60	9.48	10.07
FeO*	(wt%)	7.84	7.69	7.90	9.32
MgO	(wt%)	0.01	0.00	0.01	0.01
MnO	(wt%)	0.25	0.23	0.24	0.28
CaO	(wt%)	0.23	0.35	0.41	0.55
Na_2O	(wt%)	3.86	5.98	7.23	7.44
K_2O	(wt%)	6.04	4.64	4.21	4.65
P_2O_5	(wt%)	0.07	0.06	0.03	0.10
H_2O	(wt%)		5.75	3.45	

*Total Fe content reported as FeO

Table 4

Suswa oxidation

Sample	Suswa-01A	Suswa-01B	Suswa-03A	Suswa-03B	Suswa-03C	Suswa-11C
$Fe^{3+}/\Sigma fe^{a}$	0.16	0.18	0.18	0.17	0.17	0.17
$S^{6+}/\Sigma S$	0.05	0.15	0.16	0.08	0.10	0.11
$fO_2{}^{b}$	-0.43	-0.13	-0.10	-0.36	-0.22	-0.20
$fO_2{}^{c}$	0.41	0.68	0.69	0.53	0.58	0.60
$fO_2{}^{d}$	-0.72	-0.43	-0.42	-0.59	-0.54	-0.52

[a] calculated Fe3+/ΣFe after Muth & Wallace., (2021)

[b] fO_2 calculated after Kress and Carmichael., (1991)

[c] fO2 calculated after Jugo et al., (2009)

[d] fO2 calculated after Klimm et al., (2012)